

# Daily soil moisture mapping at 1 km resolution based on SMAP data for desertification areas in Northern China

Pinzeng Rao<sup>1,2</sup>, Yicheng Wang<sup>2</sup>, Fang Wang<sup>2\*</sup>, Yang Liu<sup>2</sup>, Xiaoya Wang<sup>3</sup>, Zhu Wang<sup>2</sup>

<sup>1</sup>State Key Laboratory of Hydrosience and Engineering, Department of Hydraulic Engineering, Tsinghua University, Beijing 100084, China.

<sup>2</sup>State Key Laboratory of Simulation and Regulation of Water Cycle in River Basin, China Institute of Water Resources and Hydropower Research, Beijing 100038, China.

<sup>3</sup>State Key Laboratory of Remote Sensing Science, Faculty of Geographical Science, Beijing Normal University, Beijing 100875, China.

\*Correspondence to: Fang Wang (657563390@qq.com)

**Abstract:** Land surface soil moisture (SM) plays a critical role in hydrological processes and terrestrial ecosystems in desertification areas. Passive microwave remote sensing products such as the Soil Moisture Active Passive (SMAP) have been shown to monitor surface soil water well. However, the coarse spatial resolution and lack of full coverage of these products greatly limit their application in areas undergoing desertification. In order to overcome these limitations, a combination of multiple machine learning methods, including multiple linear regression (MLR), support vector regression (SVR), artificial neural networks (ANN), random forest (RF) and extreme gradient boosting (XGB), have been applied to downscale the 36 km SMAP SM products and produce higher spatial-resolution SM data based on related surface variables, such as vegetation index and surface temperature. Desertification areas in Northern China, which are sensitive to SM, were selected as the study area, and the downscaled SM with a resolution of 1 km on a daily scale from 2015 to 2020 was produced. The results showed a good performance compared with in situ observed SM data, with an average unbiased root mean square error value of 0.057 m<sup>3</sup>/m<sup>3</sup>. In addition, their time series were consistent with precipitation and performed better than common gridded SM products. The data can be used to assess soil drought and provide a reference for reversing desertification in the study area. This dataset is freely available at <https://doi.org/10.6084/m9.figshare.16430478.v6> (Rao et al., 2022).

**Keywords:** Soil moisture; SMAP; Multiple machine learning; Surface variables; Desertification areas.

## 1. Introduction

Surface soil moisture (SM) plays a very important role in water-energy cycle processes (Sandholt et al., 2002; De Santis et al., 2021) and is an important source of water for plants and soil microbes (Wang et al., 2007; Gu et al., 2008; Mallick et al., 2009). Large-scale areas of northern China are undergoing desertification because of scarce precipitation and insufficient SM. The accurate acquisition of SM is valuable to ecological conservation and revegetation in arid areas of Northern China.

In the past, SM data were mainly obtained through ground measurements or the assimilation of products based on land surface models such as the Global Land Data Assimilation System (GLDAS) (Fang and Lakshmi, 2014; Zawadzki and Kędzior, 2016; Liu et al., 2021). Although most accurate SM data at different soil depths can be obtained, field measurements and in

situ observations are limited due to the high cost and labor intensity involved in their collection and are generally not representative of soil water status over larger areas (Rahimzadeh-Bajgiran et al., 2013; Zhao et al., 2018; Bai et al., 2019). With the development of remote sensing technologies, continuous SM estimates can be generated at regional and global scales (Peng et al., 2021). Compared to ground measurements, remote sensing products can provide good spatial and temporal coverage of SM with a relatively low cost to the user (Zeng et al., 2015; Zhao et al., 2018; Meng et al., 2020). Data assimilation SM products largely depend on the accuracy of the land surface model and the original inputs (Zawadzki and Kędzior, 2016). They generally have low accuracy in areas where ground measurements are scarce, which is a problem that can be overcome with remote sensing.

At present, there are many remotely sensed SM data, some of which are from microwave remote sensing satellites, including active and passive types. SM retrievals from active sensors like Synthetic Aperture Radar (SAR) are sensitive to scattering and greatly affected by the surface roughness and vegetation types (Lievens et al., 2011; Wagner et al., 2013). Unlike active sensors, passive microwave radiometers or sensors are rarely affected by scattering (Abbaszadeh et al., 2019). Common passive microwave SM products are listed in Table 1 below. Studies have compared these products and found that SMAP SM products have higher accuracy and robustness than other remotely sensed SM products (Liu et al., 2019; Wang et al., 2021).

**Table 1: Information of five common passive microwave soil moisture (SM) products.**

SM Datasets (Abbreviation)	Name	Production source	Resolution	Temporal Coverage	Equator Crossing Time
AMSR-E/Aqua Daily L3	Advanced Microwave Scanning Radiometer-Earth Observing System	National Aeronautics and Space Administration (NASA) National Snow and Ice Data Center Distributed Active Archive Center (NSIDC)	25 km; Daily	2002-2011	1:30 PM Ascending 1:30 AM Descending 6:00 PM
SMOS	Soil Moisture and Ocean Salinity	European Space Agency (ESA)	25 km; Daily	2010-present	Ascending 6:00 AM Descending 1:40 PM
FY3B	Fengyun-3B	National Satellite Meteorological Center	25 km; Daily	2011-present	Ascending 1:40 AM Descending 1:30 PM
GCOM-W1/AMSR2	Advanced Microwave Scanning Radiometer 2	Japan Aerospace Exploration Agency (JAXA)	0.25°/0.1°; Daily	2012-present	Ascending 1:30 AM Descending 6:00 PM
SMAP	Soil Moisture Active Passive	National Aeronautics and Space Administration (NASA)	36 km; Daily	2015-present	Ascending 6:00 AM Descending

Passive microwave SM products have been applied at watershed and national scale (Fang and Lakshmi, 2014; Meng et al., 2020). However, due to their coarse spatial resolution, microwave SM products have limited applicability to small-scale areas. Compared to microwave sensors, optical satellites such as MODIS and Landsat have a finer spatial resolution. Some observations generated from optical satellites provide good information about SM, such as vegetation index (VI) (usually Normalized Difference Vegetation Index (NDVI) or Enhanced Vegetation Index (EVI)) and land surface temperature (LST)

53 (Wang et al., 2007; Sun et al., 2012). Many experiments have tried to use these two parameters from optical remote sensing to  
54 retrieve surface SM (Mallick et al., 2009; Fang et al., 2013). Based on the LST and VI triangle space, Sandholt et al. (2002)  
55 proposed the temperature vegetation dryness index (TVDI) and used it to assess the SM status. Relative SM indicators can be  
56 calculated using optical remote sensing data, however, reliable ground measurements or other data are still required to obtain  
57 the true value of SM.

58 Some studies have tried to use surface variables from optical observations to improve the spatial resolution of passive  
59 remotely sensed SM products (Peng et al., 2017). Zhao et al. (2017) used the triangle method and Landsat satellite observations  
60 to disaggregate coarse-resolution SM data. Studies have shown that polynomial regression is effective in SM and optical  
61 observations (Zhao and Li, 2013; Piles et al., 2016). However, these methods have shortcomings in representing the nonlinear  
62 relationship between SM and other surface variables (Zhao et al., 2018; Hu et al., 2020). Machine learning methods can be  
63 applied to show the nonlinear relationships between SM and surface variables. Random forest (RF) and artificial neural  
64 network (ANN) have been widely used in previous studies due to their high generalization ability and robustness (Yao et al.,  
65 2017; Liu et al., 2020; Demarchi et al., 2020; Chen et al., 2021). Chen et al. (2021) developed the global surface SM dataset  
66 covering 2003–2018 at 0.1° resolution with neural networks and some related variables. Im et al. (2016) used machine learning  
67 approaches (RF, boosted regression trees, and Cubist) to downscale AMSR-E SM data in South Korea and Australia and found  
68 RF to be superior to the other downscaling methods. Although these machine learning methods perform well in constructing  
69 nonlinear regression models, there are still some shortcomings. For example, neural networks are prone to overfitting when  
70 the sampling is inefficient (Piotrowski and Napiorkowski, 2013) or variables that are weakly correlated with the dependent  
71 variable (Elshorbagy and Parasuraman, 2008; Ågren et al., 2021). Since the RF algorithm uses random sampling with  
72 replacement, its simulation results will not exceed the range of training set and tend to ignore some extreme values when used  
73 as a regression model (Belgiu and Drăguț, 2016). Additionally, it does not perform well when learning from an extremely  
74 imbalanced training data (Lin et al., 2021). Extreme gradient boosting (XGB), as a new ensemble learning method (Chen and  
75 Guestrin, 2016), performs well in some fields (Wang et al., 2020; Fan et al., 2021; Ma et al., 2021), but it has rarely been used  
76 for soil moisture downscaling. Compared with methods such as RF, the XGB algorithm adopts the boosting weighted sampling  
77 method, which can reduce the impact of imbalanced data and better simulate the extreme values existing in the samples (Chen  
78 and Guestrin, 2016). The coarse-resolution remote sensed SM (>10 km) itself has ignored some maxima or minima with  
79 relatively finer-grid SMs, so a method that better simulates extreme values will obviously have certain theoretical advantages.

80 The selection of feature variables is critical for regression models. In addition to LST and VI mentioned above, variables  
81 such as terrain and soil conditions also have a significant impact on SM. Abbaszadeh et al. (2019) downscaled SMAP  
82 radiometer SM products over the continental United States using MODIS products (including NDVI and LST), precipitation  
83 and topographic data, and evaluated the influence of soil texture on SM. Zhao et al. (2018) added additional surface variables,  
84 such as leaf area index (LAI), normalized difference water index (NDWI), surface albedo and the solar zenith angle. Hu et al.  
85 (2020) added the normalized shortwave-infrared difference bare soil moisture index (NSDSI), horizontally polarized

86 Brightness Temperature (TBh) and vertically polarized Brightness Temperature (TBv) to the regression model. In general, all  
87 these variables can be classified into vegetation, temperature, soil wetness, topography, and soil factors and sensors conditions.

88 In recent years, the Chinese government has carried out afforestation activities in order to reverse desertification in the  
89 North. Considering the role of SM in terrestrial ecosystems, it is urgent to obtain accurate SM with high temporal and spatial  
90 resolution. This study aims to downscale SMAP SM products by constructing a nonlinear relationship between SM and related  
91 surface variables by means of multiple machine learning methods and generate SM products with higher temporal and spatial  
92 resolution in desertification areas. The in situ observed SM data from the Maqu Monitoring Network and Babao Monitoring  
93 Network, several gridded SM products, and precipitation and temperature data from meteorological stations were used for  
94 validation and analysis.

## 95 **2. Materials and methodology**

### 96 **2.1 Study area**

97 Northern China is mostly arid with an annual precipitation of generally less than 600 mm, and is subject to large-scale  
98 desertification. The desert areas of Northern China are susceptible to climate and hydrological changes and have fragile  
99 ecosystems. Soil water is a key parameter in land-atmosphere interactions (Ma et al., 2019), and its change greatly affects the  
100 survival of vegetation and agricultural production in desertification areas. The studied area whose boundaries are provided by  
101 government departments used for this study covers 3.36 million km<sup>2</sup>, encompassing seven provinces (Fig. 1). The precipitation  
102 in the study area decreases gradually from southeast to northwest, and belongs to the temperate continental climate (Fig. 1).  
103 The terrain is complex, and the average elevation is approximately 1,900 m, ranging from -192 m to 7,439 m.

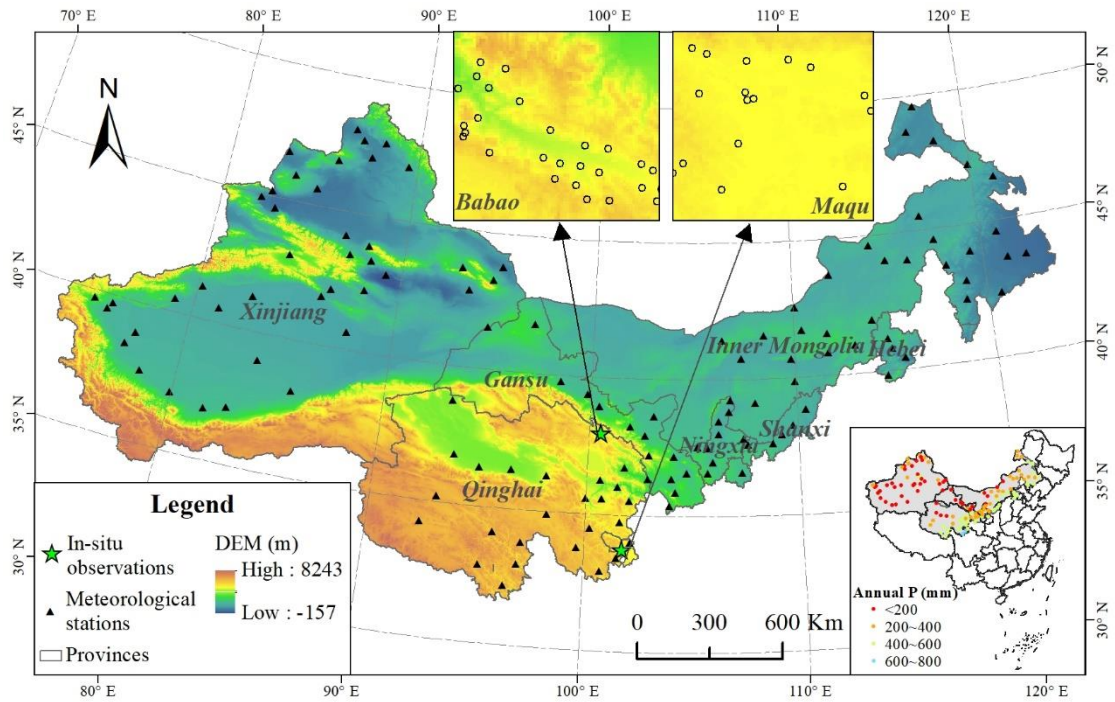


Figure 1: Location of the study area.

## 2.2 Observations for the production of soil moisture data

### 2.2.1 SMAP SM data

The SMAP satellite was launched on January 31, 2015. Its mission consists of an L-band radar and radiometer instrument suite, which provides global measurements and monitoring of SM in the top 5 cm of soil. The Level-3 products are daily composites of the Level-2 products and are the most commonly used for applications. The Level-3 products are available in three spatial resolutions: 36 km passive, 9 km active-passive, and 3 km active (O'Neill et al., 2010). Following the malfunctioning of its radar in 2015, SMAP radar data were replaced with those of Sentinel-1, limiting the application of active and active-passive products.

The SMAP Level-3 passive daily SM product (L3\_SM\_P, Version 6) with a grid resolution of 36 km has been produced since March 31, 2015. Zeng et al. (2015) showed that most of remotely sensed SM products were slightly better during daytime than during nighttime, and the same conclusion for the SMAP SM product was confirmed by Zhao et al. (2018). Therefore, the SMAP Level-3 SM product with the descending overpass time of 6:00 AM was used in this study. The data were downloaded from NASA Earthdata (<https://search.earthdata.nasa.gov>).

### 2.2.2 MODIS products

120 MODIS provides continuous time-series predictors for important parameters, such as vegetation index and surface  
121 temperature. This paper used MODIS products MOD09A1, MOD11A1, MOD13A2, MOD15A2H and MCD43D58 (Table 2).  
122 The 1-km daily LST was provided by MOD11A1, and the 1-km 16-day EVI and NDVI was provided by MOD13A2.  
123 MOD15A2H provided 8-day Leaf Area Index (LAI) with a spatial resolution of 500 m. MCD43D58 provided daily albedo  
124 data with a spatial resolution of 30 arc second (~1,000 m). Some soil wetness related indexes, including NDWI, NSDSI, and  
125 Land Surface Water Index (LSWI), were produced by MOD09A1. Their formulas are:

$$126 \quad NDWI = (B_4 - B_2)/(B_4 + B_2) \quad (1)$$

$$127 \quad LSWI = (B_2 - B_6)/(B_2 + B_6) \quad (2)$$

$$128 \quad NSDSI = (B_6 - B_7)/B_6 \quad (3)$$

129 where  $B_2$ ,  $B_4$ ,  $B_6$  and  $B_7$  represent the MOD09A1 surface reflectance of the 2nd, 4th, 6th and 7th bands, respectively.

130 These MODIS products are available from NASA Earthdata (<https://search.earthdata.nasa.gov>). All data were obtained  
131 from 2015 to 2020 and processed to a spatial resolution of 1,000 meters.

### 132 **2.2.3 Topographic data**

133 Topographic factors are strongly related to SM, including elevation, slope and aspect (Bai et al., 2019; De Santis et al.,  
134 2021). The Shuttle Radar Topography Mission (SRTM) digital elevation model (DEM) at 3 arc second resolution (~100 m),  
135 version 3, obtained from the Land Processes Distributed Active Archive Center (LP  
136 DAAC)( <https://e4ftl01.cr.usgs.gov/MEASURES/SRTMGL3.003/>), was used as elevation. Slope and aspect were generated  
137 based on the DEM.

### 138 **2.2.4 Soil texture data**

139 Soil texture, the proportions of sand, silt and clay particles, controls the water holding capacity of the soil. The soil data  
140 at 1,000 m resolution, including the proportions of sand, silt and clay, used for this study used the China Soil Characteristics  
141 Dataset (CSCD) (Shangguan et al., 2012), obtained from National Tibetan Plateau Data Center (<http://westdc.westgis.ac.cn/>).

### 142 **2.2.5 In Situ SM observations**

143 The in situ SM measurements were collected from the data provided by the Maqu Monitoring Network (Zhang et al.,  
144 2020) and the Babao Monitoring Network (Kang et al., 2017). The Maqu Monitoring Network covers 26 sites and provides  
145 SM for the surface layer (0-5 cm) at 15-minute intervals from 2009 to 2019; 19 of the available sites which have data after  
146 2015 were used in this study (Fig. 1). The Babao Monitoring Network covers 40 sites and provides hourly SM for the surface  
147 layer (4 cm, 10 cm and 20 cm) from 2013 to 2017; 29 of the available sites have data after 2015 and their observations of the  
148 first layer (4 cm) were used in this study (Fig. 1). To compare with the simulated results, they were all processed into daily  
149 time series.

## 150 2.2.6 Precipitation and temperature data

151 The daily precipitation and temperature data were acquired from 131 meteorological stations from the China  
 152 Meteorological Data Service Centre (<http://data.cma.cn>). The spatial locations of these meteorological stations are shown in  
 153 Fig. 1. The average annual precipitation of most stations from 2015 to 2020 is less than 600 mm, and gradually decreases from  
 154 northwest to southeast (Fig. 1).

155 **Table 2: Main predictors used in the study and corresponding datasets**

Datasets	Predictors	Original spatial resolution	Temporal resolution	Number of granules (Years×tiles)
SMAP	SM	~36 km	Daily	2,064
MOD11A1	LST	1 km	Daily	17,460
MOD13A2	NDVI; EVI	1 km	16-day	1,104
MOD15A2H	LAI; FAPAR	500 m	8-day	2,208
MOD09A1	NDWI; LSWI; NSDSI	500 m	8-day	2,208
MCD43D58	Albedo	30 arc second (~1 km)	Daily	2,192
SRTM	DEM; Slope; Aspect	3 arc second (~100 m)	-	32
CSCD	Sand; Silt; Clay	1 km	-	1

## 156 2.2.7 Other gridded SM datasets

157 Some other gridded SM data were used to compare the simulation results (Table 3). The SMAP Level-2 product  
 158 (L2\_SM\_SP) merges SMAP radiometer and processed Sentinel-1A/1B SAR observations. It is available at 3 km and 1 km  
 159 resolutions. The Global Change Observation Mission Water (GCOM-W1) AMSR2 product is produced by the Japan  
 160 Aerospace Exploration Agency (JAXA), and SM data at a 0.1° spatial resolution were selected for this study. The Copernicus  
 161 Climate Change Service (C3S) produces a global SM gridded dataset from 1978 to present from satellite sensors such as SMOS,  
 162 AMSR2 and SMAP. It has a spatial resolution of 0.25 degrees and offers three types of products: active, passive and combined.  
 163 The combined product that we used in this study is generated by merging the active and passive products. The fifth generation  
 164 reanalysis dataset (ERA5) produced by European Centre for Medium-Range Weather Forecasts (ECMWF) provides several  
 165 variables including volumetric soil water over several decades. In this dataset, the soil is divided into four layers and the depth  
 166 of the top layer is 0-7 cm. In this study, we downloaded the hourly volumetric soil water data of the top layer and processed  
 167 them as daily averages. Famine Early Warning Systems Network (FEWS NET) Land Data Assimilation System (FLDAS)  
 168 provides daily SM at a 0.01° spatial resolution over the Central Asia region (30-100° E, 21-56° N), which covers part of our  
 169 study area. The product consists of four layers of SM, and the SM at the top layer (0-10 cm) was selected for this study.

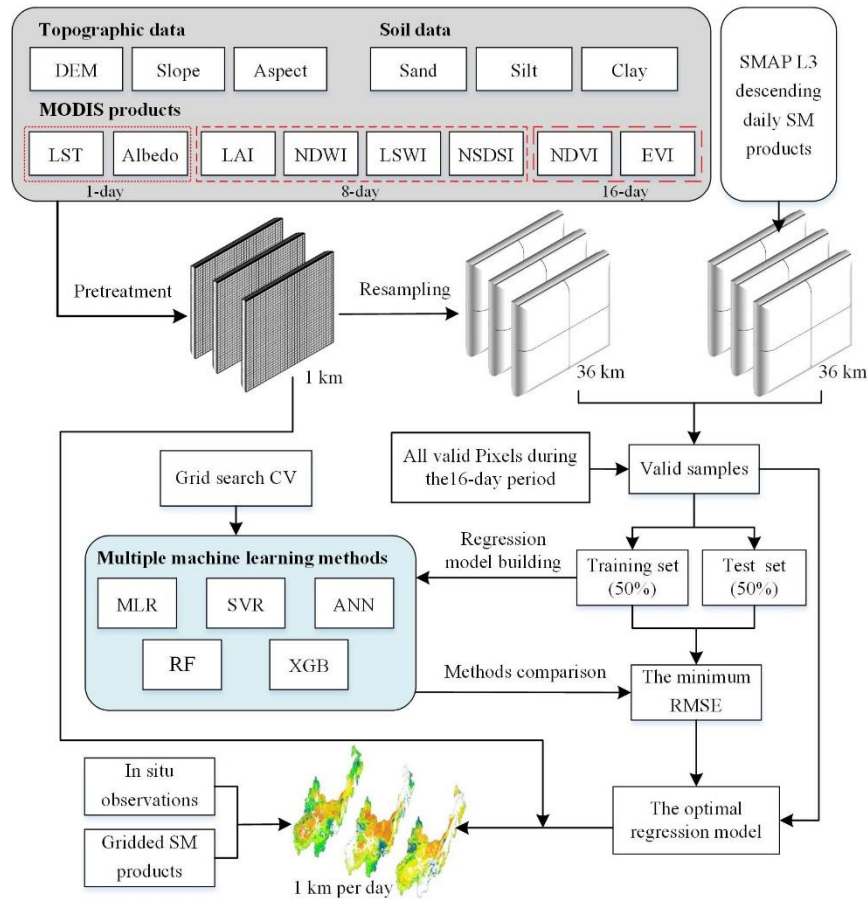
170 **Table 3: The gridded SM products used in this study**

Institution	Name	Soil layers	TYPES	Temporal resolution	Grid spacing	Data link
NASA	SMAP/ Sentinel-1 (L2_SM_SP)	One layer (0-5 cm)	Active microwave	1-2 days	1/3 km	<a href="https://cmr.earthdata.nasa.gov/search/concepts/C1931663473-NSIDC_ECS.html">https://cmr.earthdata.nasa.gov/search/concepts/C1931663473-NSIDC_ECS.html</a>
JAXA	GCOM-W1/AMSR2	One layer (~)	Passive microwave	Daily	0.1°/0.25° (~11 km/28 km)	<a href="https://gportal.jaxa.jp/gpr/">https://gportal.jaxa.jp/gpr/</a>
ECMWF	C3S	One layer (~)	Passive, active and combined	Daily	0.25° (~28 km)	<a href="https://cds.climate.copernicus.eu/cdsapp#!/dataset/satellite-soil-moisture">https://cds.climate.copernicus.eu/cdsapp#!/dataset/satellite-soil-moisture</a>

ECM WF	ERA5	Four layers (0-7 cm, 7-28 cm, 28-100 cm, 100-289 cm)	Reanalysis	Hourly	0.1°(~11 km)	<a href="https://cds.climate.copernicus.eu/cdsapp#!/dataset/reanalysis-era5-land">https://cds.climate.copernicus.eu/cdsapp#!/dataset/reanalysis-era5-land</a>
NAS A	FLDAS	Four layers (0-10 cm, 10-40 cm, 40-100 cm, 100-200 cm)	Reanalysis	Daily	0.01°(~1.1 km)	<a href="https://cmr.earthdata.nasa.gov/search/concepts/C2020764153-GES_DISC.html">https://cmr.earthdata.nasa.gov/search/concepts/C2020764153-GES_DISC.html</a>

171 **2.3 Downscaling approach based on multi-machine learning**

172 According to the selected variable indicators (mainly including topographic data, soil data and some MODIS products)  
 173 and machine learning methods, we constructed a framework to downscale SMAP SM based on multiple machine learning  
 174 methods (Fig. 2).



175  
176

**Figure 2: Schematic of the SMAP soil moisture downscaling framework**



### 177 2.3.1 Machine learning methods

178 Machine learning methods are widely used in regression and classification. We selected machine learning methods that  
179 are currently widely used to build regression models for SM and its related variables. We studied five methods: multiple linear  
180 regression (MLR), support vector regression (SVR), artificial neural networks (ANN), random forest (RF) and extreme  
181 gradient boosting (XGB). MLR and SVR have been widely used as regression methods in the past (Yu et al., 2012; Achieng,  
182 2019; Wang et al., 2019). ANN is currently one of the most popular machine learning methods and is used in many fields,  
183 including the inversion of remotely sensed SM (Del Frate et al., 2003; Elshorbagy and Parasuraman, 2008; Yao et al., 2017;  
184 Chen et al., 2021).

185 RF and XGB are tree based ensemble algorithms, which have prediction accuracy and good generalization ability, and  
186 are not prone to overfitting (Rao et al., 2018; Abbaszadeh et al., 2019). RF is a multiple-tree algorithm improved by bootstrap  
187 to reduce decision tree bias in determining the splits (Mohana et al., 2021). Several studies have used RF to build regression  
188 models of remotely sensed SM and related variables, and almost all achieved better results compared to other regression  
189 methods (Zhao et al., 2018; Qu et al., 2019; Hu et al., 2020). In contrast, the application of XGB, which applies a regularized  
190 gradient boosting framework, is still very limited. However, XGB has prominent advantages in generalization performance  
191 and accuracy (Wang et al., 2020).

192 The XGB algorithm is a boosting-type ensemble of multiple CART decision trees (Chen and Guestrin, 2016). The  
193 predicted result of the boosting-type tree ensemble model can be expressed as follows:

$$194 \hat{y}_i = \Phi(x_i) = \sum_{k=1}^K f_k(x_i), f_k \in F \quad (4)$$

195 where  $F$  is the space of regression tree,  $K$  is the total number of trees, which means the model uses  $K$  additive functions,  
196  $f_k(x_i)$  is the weighted score of the  $k$ -th tree on  $i$ -th input data ( $x_i$ ).

197 XGB adopts a regularized learning objective to optimize the simulation results.

$$198 Obj(\Phi) = \sum_{i=1}^N l(y_i, \hat{y}_i) + \sum_{k=1}^K \Omega(f_k) \quad (5)$$

199 where  $l$  is the loss function,  $N$  is the total number of input,  $\Omega$  is the regularization term to penalize the model complexity and  
200 prevent overfitting.

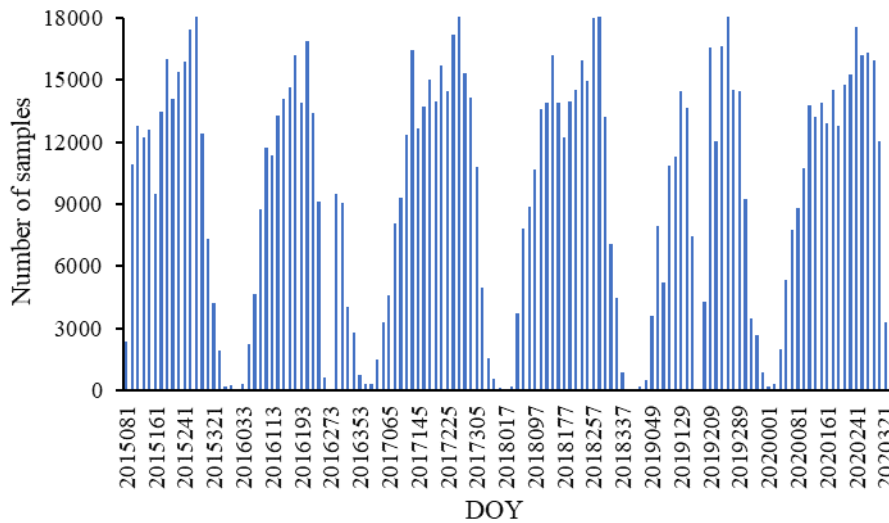
201 Compared with RF and other some methods, XGB has significantly faster calculation speed (Fan et al., 2018; Shi et al.,  
202 2021). Some studies have shown that XGB is a better regression and classification algorithm than RF and other machine  
203 learning methods (Ågren et al., 2021; Fan et al., 2021).

### 204 2.3.2 The construction of 16-day regression model

205 The downscaling process is shown in Fig. 2. First, all data need to be preprocessed. Daily LST data are likely to be  
206 affected by the cloud, so we performed quality control to MOD11A1 products using its quality control (QC) band and choose  
207 high-quality cloud-free pixels. All selected variables, including LST, Albedo, LAI, NDWI, LSWI, NSDSI, NDVI, EVI, DEM,

208 slope, aspect, sand, silt and clay, were aggregated into a resolution of 1 km with a geotiff format. These variables were further  
209 resampled to the spatial resolution of the SMAP SM data (36 km) using the nearest neighbor interpolation method.

210 Second, valid samples were obtained and split. Since it is severely affected by noise (such as clouds), MOD11A1 only  
211 provides daily valid clear-sky LST values onto grids. In addition, each SMAP image has a narrow coverage and provides only  
212 a small number of valid pixels per day. It means that there may be few or no valid samples if only the data of a certain day are  
213 selected to build the regression. The variables from MOD13A2 and MOD15A2H are the best composite within 16 days and 8  
214 days, respectively. To overcome the limitation, we chose to build regression models within 16 day periods (the lowest temporal  
215 resolution from these dynamic variables). All valid data (including training and test sets) within 16 days were used as the  
216 samples in the regression model. For instance, for NDVI and EVI on January 1, 2020, which are composite results from January  
217 1st to 15th, the valid data during the period were used as samples. The number of valid samples for surface variables and  
218 SMAP SM for each period in 2015-2020 is shown in Fig. 3. The day of year (DOY) is used to represent the corresponding  
219 period. Since limited available SMAP SM grid data, there may be few valid samples we can obtain during cold seasons. The  
220 valid samples for each period were divided into training and test sets, each accounting for 50% of the total number of samples.  
221 In this study, stratified random sampling based on sampling date during the 16-day period was employed to split the training  
222 and test sets. Moreover, to avoid excessively inconsistent training and test sets, the Kolmogorov-Smirnov (KS) test is adopted  
223 to test the distribution consistency of them (Kovalev and Utkin, 2020). If the p-value of the KS test result is less than or equal  
224 to 0.05, stratified random sampling is performed again, and until the requirements are met.



225

226 **Figure 3: The number of valid samples for a 16-day period in 2015-2020. DOY is the day of year, the same below.**

227 Third, the regression model was determined based on training and test sets. Considering the number of samples is critical  
228 to the accuracy of the regression model, we only selected periods with more than 100 samples to build the model and DOY of  
229 2016017, 2018017, 2018353, 2019001 and 2019177 were excluded. Then, we used the training set and multiple machine

230 learning methods (MLR, SVR, ANN, RF and XGB) to build a regression model for each 16-day period. The regression model  
 231 was then defined according to the selected machine learning method:

$$232 \quad SM = f(LST, Albedo, LAI, NDWI, LSWI, NSDSI, NDVI, EVI, \\ 233 \quad DEM, slope, aspect, sand, silt \text{ and } clay) \quad (6)$$

234 where  $f$  represents the regression function of the machine learning method (MLR, SVR, ANN, RF or XGB).

235 Finally, hyperparameter turning and the selection of the optimal model. Hyperparameters are critical for some machine  
 236 learning methods (Klein et al., 2017; Khan et al., 2020; Sun et al., 2021). In this study, the key hyperparameters of SVR, ANN,  
 237 RF and XGB are tuned based on grid search cross-validation (CV). All models are evaluated based on the correlation  
 238 coefficient (R) and the root mean square error (RMSE). They are calculated as follows:

$$239 \quad R = \frac{Cov(SM_I, SM_P)}{\sqrt{Var(SM_I)Var(SM_P)}} \quad (7)$$

$$240 \quad RMSE = \sqrt{\frac{1}{n}(SM_P - SM_I)^2} \quad (8)$$

241 where  $SM_I$  is the SMAP SM,  $SM_P$  is the corresponding SM predicted by the regression model,  $Cov$  represents the covariance  
 242 function,  $Var$  is the variance, and  $n$  is the number of valid samples for  $SM_I$  or  $SM_P$ .

243 The RMSE is used as the evaluation metric for hyperparameter turning. The tuning results of hyperparameters are shown  
 244 in Tables S2 and S3. According to the optimal hyperparameter, the corresponding model can be constructed.

### 245 **2.3.3 Prediction of 1-km daily SM product**

246 The accuracy of the five regression models was compared using the average RMSE of training and test sets. This average  
 247 RMSE can be expressed as:

$$248 \quad \overline{RMSE} = \frac{RMSE_{Training} + RMSE_{Test}}{2} \quad (9)$$

249 where  $RMSE_{Training}$  and  $RMSE_{Test}$  are the RMSE of training and test sets for these models, respectively.

250 The regression model with the smallest  $\overline{RMSE}$  was selected as the optimal model. Furthermore, we used the selected  
 251 optimal model and these surface variables with a resolution of 1 km within 16 days to simulate daily SM at 1 km resolution  
 252 on the corresponding date. Taking 16 days as a period, all daily SM data with a spatial resolution of 1 km from 2015 to 2020  
 253 were predicted. In addition, to obtain a more complete time series of SM data, we used the model of the previous period when  
 254 the number of valid samples was less than 100.

### 255 **2.4 Evaluation method**

256 The in situ SM measurements were used to validate the downscaled results. In addition to R and RMSE, bias and unbiased  
 257 RMSE (ubRMSE) were also used for accuracy evaluation. Bias indicates the overall level of overestimation or underestimation  
 258 of simulation results. ubRMSE can eliminate the influence of deviation. They were calculated according to:

259 
$$ubRMSE = \sqrt{\frac{1}{n}((SM_{In} - \overline{SM_{In}}) - (SM_D - \overline{SM_D}))^2}$$
 (10)

260 
$$bias = \overline{SM_{In}} - \overline{SM_D}$$
 (11)

261 where  $SM_{In}$  is the in situ observed SM,  $SM_d$  is the downscaled SM of the corresponding grid, and  $n$  is the number of valid  
 262 samples for  $SM_{In}$  or  $SM_D$ .

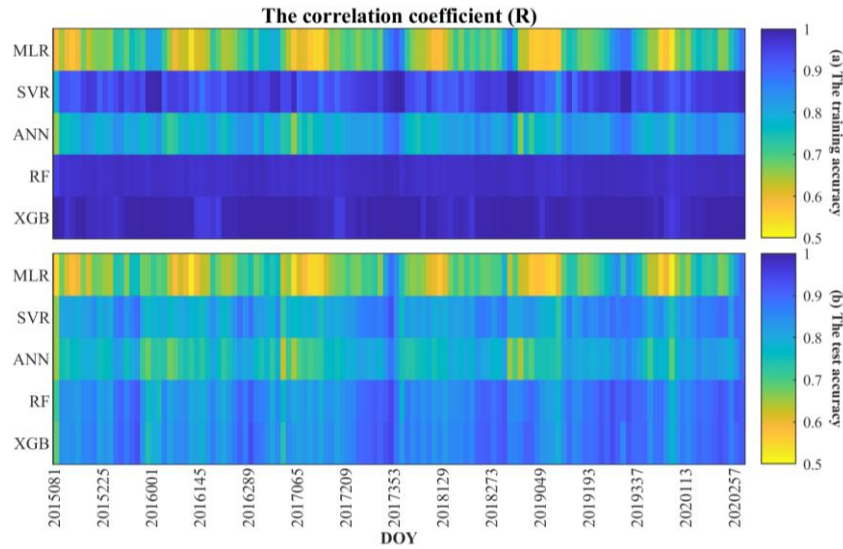
263 **3. Results**

264 **3.1 Model comparison**

265 The daily SM data from DOY 81 in 2015 to DOY 366 in 2020 were simulated producing 128 regression results every 16  
 266 days. The correlation coefficient (R) and the root mean square error (RMSE) of each regression result for the training set and  
 267 the test set are shown in Fig. 4 and Fig. 5, respectively. According to Equation 9, among the 128 regression results, there were  
 268 114 from the XGB model, and 14 from RF.

269 For all models except MLR, R is greater than 0.6 and RMSE is less than 0.05 m<sup>3</sup>/m<sup>3</sup> both for training and test sets. R  
 270 values greater than 0.6 and 0.8 indicate reliable and strong correlations, respectively (Akoglu, 2018). It means that all methods  
 271 except MLR have reliable simulation accuracy. For the training set using XGB, Rs are all above 0.96, generally higher than  
 272 for other methods; Similarly, the RMSEs of XGB are all lower than 0.02 m<sup>3</sup>/m<sup>3</sup>, generally lower than those of other methods.  
 273 The R of RF is second only to that of XGB, and for several periods it is higher than for XGB; the RMSEs of RF are also  
 274 generally lower than 0.02 m<sup>3</sup>/m<sup>3</sup> and are lower than those of XGB in several periods. SVR and ANN perform generally better  
 275 in the cold season, and worse in other seasons. In general, their results are inferior to those of XGB and RF. The simulation  
 276 results of MLR are relatively poor both in terms of RMSE and R.

277 The results of the test set show that XGB, RF and SVR perform better than ANN and MLR. Table 4 shows the average  
 278 RMSE and R values of the training and test sets over all periods, and the performance order of the model can be obtained as  
 279 XGB>RF>SVR >ANN >MLR. In addition, there are seasonal variations in R and RMSE both for training and test sets.  
 280 Moreover, the evaluation accuracy is generally better in the cold season, when sample sizes are relatively small.



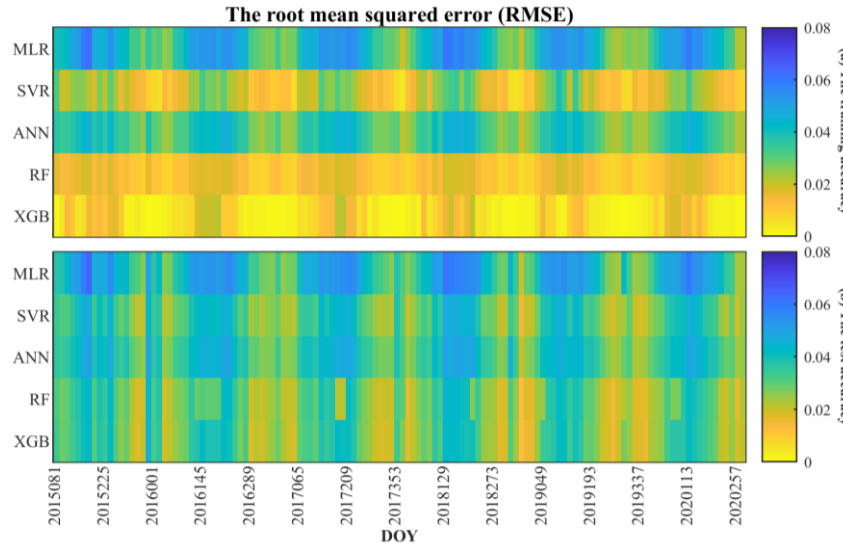
281

282

**Figure 4: The correlation coefficient (R) of the models (MLR, SVR, ANN, RF and XGB) on different periods: (a) The training**

283

**accuracy; (b) The test accuracy.**



284

285

**Figure 5: The root mean square error (RMSE) of the models (MLR, SVR, ANN, RF and XGB) for different periods: (a) The training**

286

**accuracy; (b) The test accuracy.**

287

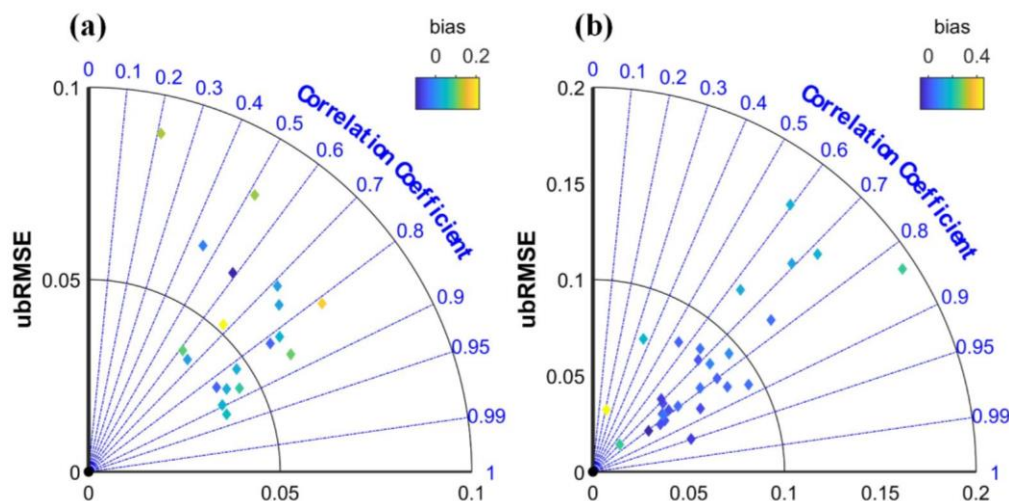
**Table 4: Accuracy of the models based on correlation coefficient (R) and root mean square error (RMSE)**

Model		MLR	SVR	ANN	RF	XGB	Combination
Training set	R	0.688	0.943	0.864	0.978	0.991	0.992
	RMSE (m <sup>3</sup> /m <sup>3</sup> )	0.042	0.019	0.028	0.013	0.007	0.007
Test set	R	0.675	0.824	0.660	0.857	0.861	0.861
	RMSE (m <sup>3</sup> /m <sup>3</sup> )	0.043	0.033	0.047	0.030	0.029	0.028

288

### 3.2 Comparison with the in situ data and precipitation

289 The downscaled 1 km gridded SM were compared with the in situ SM observations of the Maqu Network and Babao  
 290 Network (Fig. 6). Due to the difference in sensors, soil depth and measurement scale (point observation in case of the in situ  
 291 measured SM and 1 km grid for the downscaled SM), there is a certain deviation between in situ observation data and the  
 292 downscaled gridded SM data. The downscaled SM of most sites at the Maqu Network and Babao Network are highly correlated  
 293 with the in situ measured SM ( $R > 0.6$ ). In the Maqu Network, the ubRMSEs with an average of  $0.057 \text{ m}^3/\text{m}^3$  are all less than  
 294  $0.090 \text{ m}^3/\text{m}^3$ , and the bias ranges from  $-0.10$  to  $0.22 \text{ m}^3/\text{m}^3$ . In the Babao Network, the average ubRMSE of all sites is  $0.081$   
 295  $\text{m}^3/\text{m}^3$ , and some of them exceed  $0.1 \text{ m}^3/\text{m}^3$ . In addition, their bias ranges from  $-0.07$  to  $0.45 \text{ m}^3/\text{m}^3$ . It means that the validation  
 296 accuracy of Babao Network is generally lower than Maqu Network. That may be mainly because the measured soil depth at  
 297 the Babao Network is 4 cm, which means that there could be a systematic error between the datasets. Therefore, the validation  
 298 accuracy should mainly refer to the evaluation accuracy of Maqu network.



299  
 300 **Figure 6: The relationships between in situ SM and downscaled SM. (a) Maqu Network; (b) Babao Network.**

301 To better understand the reason for these poor results, the scatter plots comparing the two sets of data were drawn. Figure  
 302 7 shows the results of the 19 sites of the Maqu Network. All four statistical metrics, namely, R, RMSE, ubRMSE and bias  
 303 were calculated, and their fitting line of the scatter was plotted. Not surprisingly, the relationship is generally improved where  
 304 there are more valid data. It means that the validation effect of in situ observations is affected by the amount of data. The same  
 305 conclusion can be drawn through 29 sites at the Babao Network (Fig. S1).

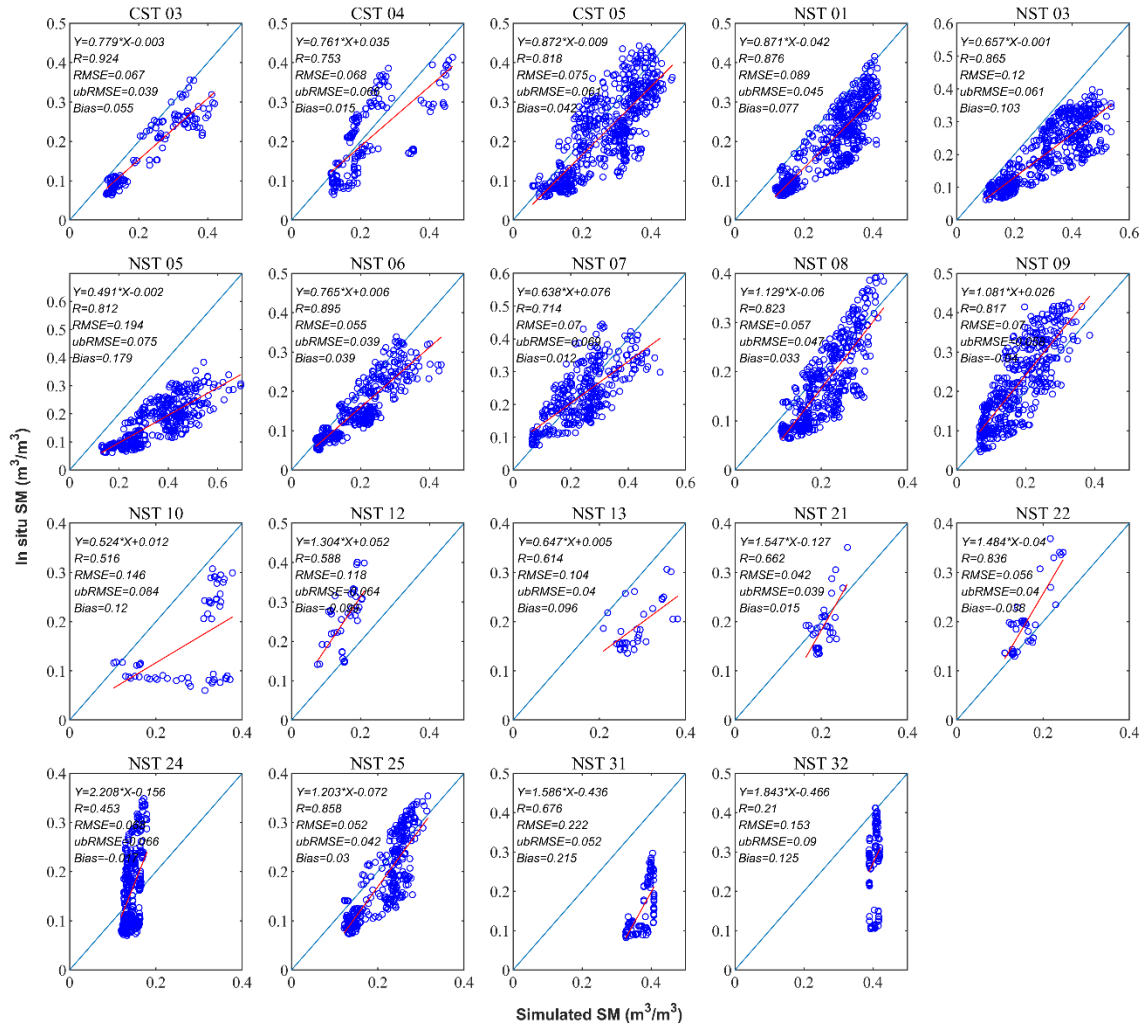


**Figure 7: Comparison between the downscaled SM and in situ SM of the Maqu Network.**

All SM products are compared with in situ SM. Figure 8 shows a significantly higher correlation between the downscaled SM and in situ SM of the Maqu Network. The median ubRMSE of the downscaled SM is the smallest, and its RMSE is second only to the C3S (0.25°) product. The bias of the downscaled SM is higher than that of some products, even higher than the original SMAP L3 (36 km) data. Almost the same results can be obtained from in situ observations of Babao Network (Fig. S2). The difference is that the bias of the downscaled SM is lower than the result of SMAP L3 (36 km). Compared with the RF-based and the XGB-based downscaled SMs, the downscaled SM with multiple machine learning approaches performed better, especially R and ubRMSE.

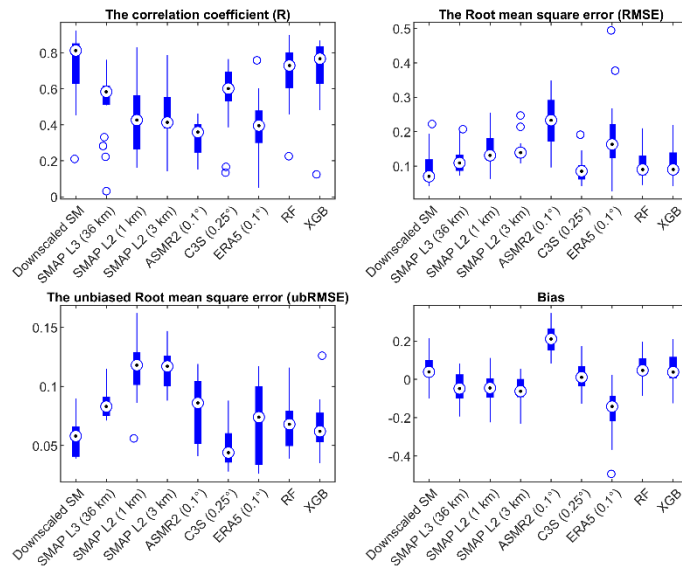
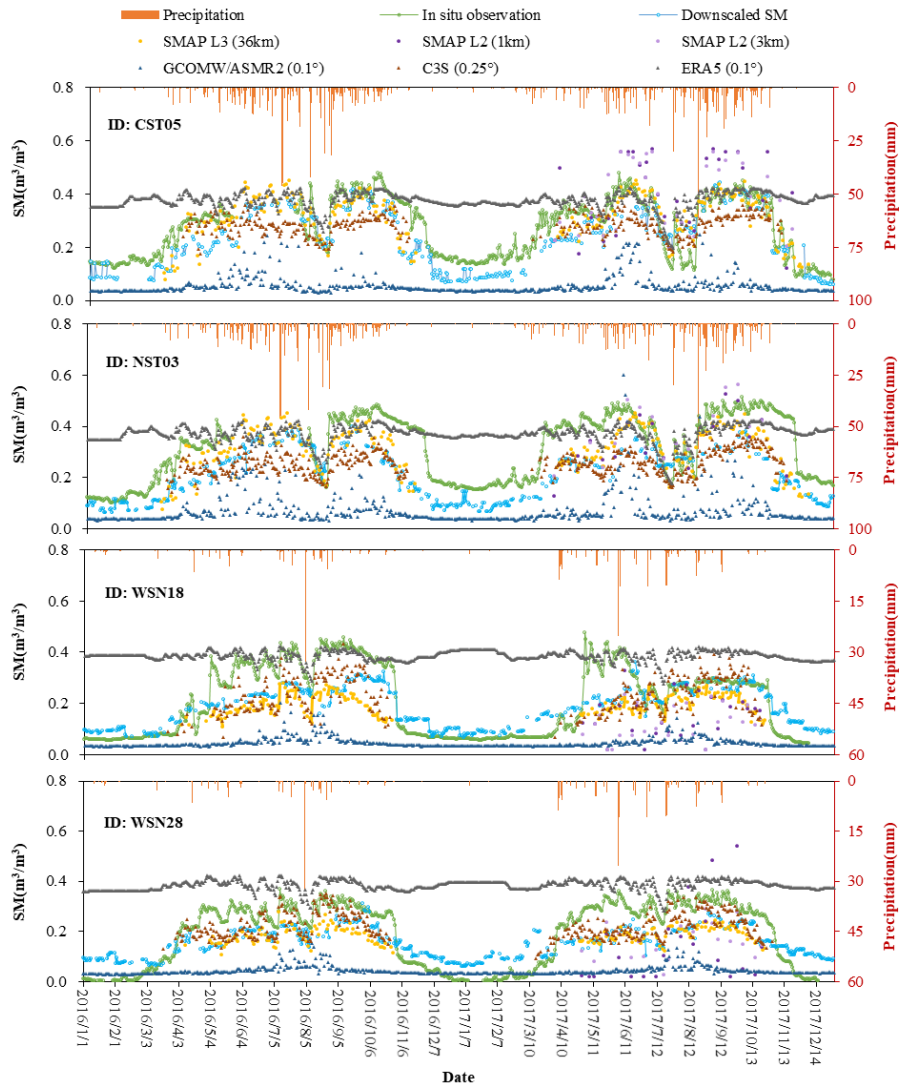


**Figure 8: Comparison of gridded products and in situ observation SM of the Maqu Network.**

The observed SM of sites with a greater number of observed data were compared with these gridded SM data at different resolutions and precipitation. Figure 9 shows the temporal variations of these SM at four sites 2016-2017. The relationship between in situ observed SM and precipitation at all four sites is very consistent, showing annual fluctuation. The greater SM corresponds to more precipitation during the hot season, and the smaller SM corresponds to less precipitation during the cold season.

Except for GCOMW/ASMR2 SM, the variation trends of these acquired gridded SM and the downscaled SM are basically the same despite the large difference in spatial resolution. GCOMW/ASMR2 significantly underestimates SM compared to other products. Both the SMAP L2 SM at 1 km and 3 km may be overestimated (CST05) and may also be underestimated (WSN18) compared with in situ observations. Moreover, SMAP L2 SM has some valid data mainly on hot days and almost no valid data during cold seasons. The peak values of the ERA5 SM are close to those of the in situ observations, but the low values are overestimated. The C3S SM is similar to the 36 km SMAP SM, and its peak values are simulated more accurately, while the minimum values have little valid data. Compared with the original data (36 km SMAP L3), the downscaled SM has a more complete time series, especially during the cold season. The downscaled SM data almost all match well with the in situ measured SM data, and all of them are consistent with the precipitation. The difference between the downscaled SM and the in situ measured SM is mainly reflected in the magnitude of the variation, which is probably due to the difference in spatial resolution.





333

334 **Figure 9: Time series of the in situ observed SM, the downscaled SM, the acquired gridded SM products and daily precipitation at**  
 335 **the four selected SM sites (From Maqu Network and Babao Network, respectively) in 2016-2017.**

336

### 3.3 Mapping of the downscaled SM

337

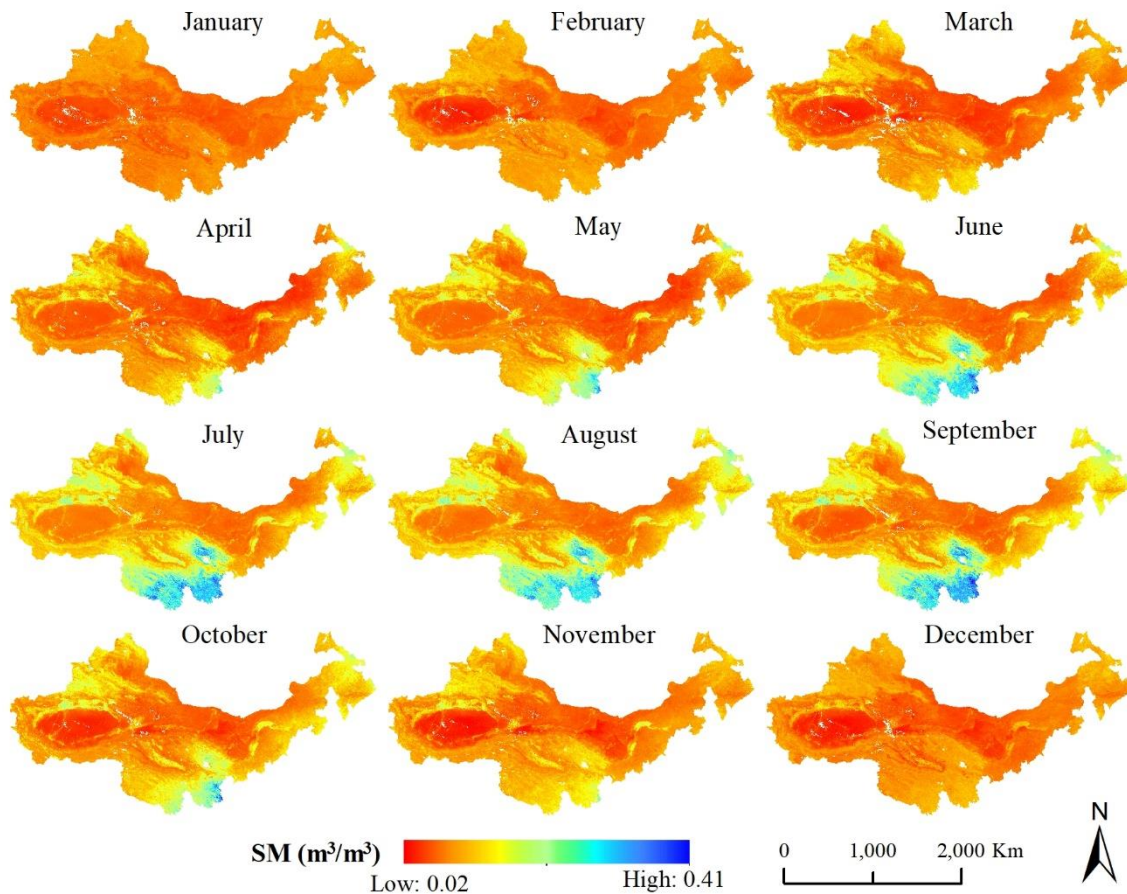
338

339

340

341

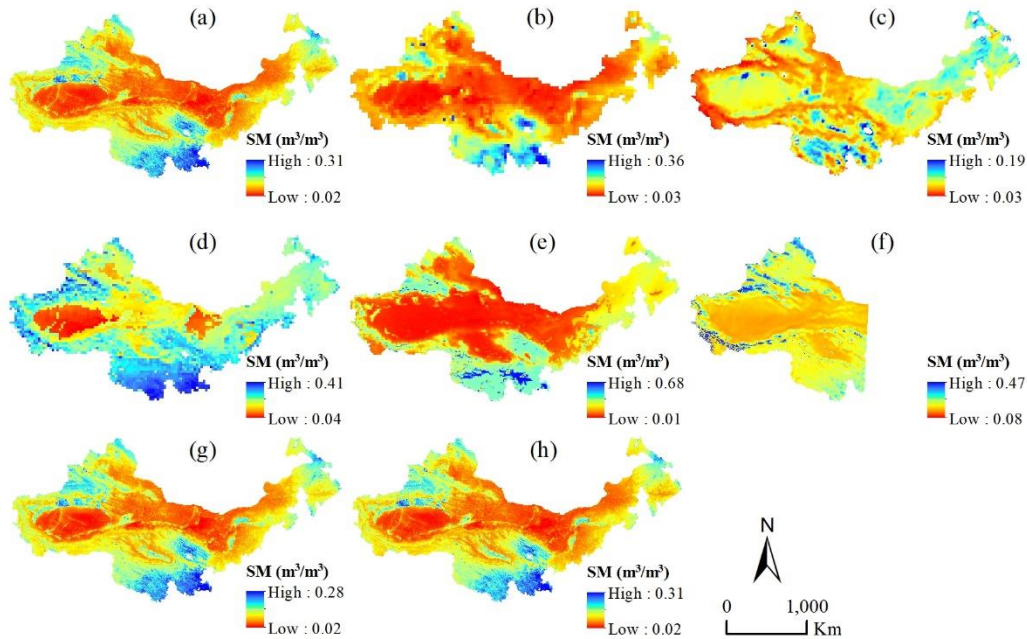
SM varies greatly in different months in desertified areas. Figure 10 shows the average SM in each month in the study area. The SM shows a monthly change pattern, and the values from June to September are bigger than in other months, especially in southern Qinghai Province, eastern Inner Mongolia Province, and western Xinjiang Province. The SM in some areas is low throughout the year, such as in the Tarim Basin of Xinjiang Province, western Inner Mongolia Province and most of Gansu Province.



342  
343 **Figure 10: Monthly average SM in the study area.**

344 The annual average SM was calculated (Fig. S3). Compared with the monthly average SM, the annual average SM  
 345 changed significantly less. Further, we compared the spatial patterns of the downscaled SM with the gridded SM products with  
 346 different resolutions. Figure 11 shows the daily average SM of these products from 2015 to 2020. The spatial patterns of the  
 347 downscaled SM and 36 km SMAP SM are basically consistent, but the downscaled data show better details in some areas such  
 348 as near rivers. The overall values of GCOMW SM are relatively small, and exhibit some obvious errors in some areas. For  
 349 example, SM in the Tarim Basin is higher than in the surrounding area, which is completely inconsistent with other SM data.  
 350 The spatial pattern of the C3S SM is close to the downscaled SM and the 36 km SMAP SM, but some details are not presented.  
 351 For example, SM in the Hetao Plain along the Yellow River is much higher than that in its surrounding area, which can be  
 352 found in the downscaled SM and the SMAP SM, but not in the C3S SM. There are obvious errors in the results of ERA5. The  
 353 average SM is significantly overestimated in the southern part of the study area, and underestimated in some areas in the  
 354 northern of the study area. The FLDAS SM has high resolution, and its overall spatial pattern is relatively consistent with the  
 355 downscaled SM and 36 km SMAP SM. The difference is that the FLDAS SM is significantly larger in higher elevation areas  
 356 of the west than in other regions, which is quite different from other products. This suggests that the FLDAS SM may be

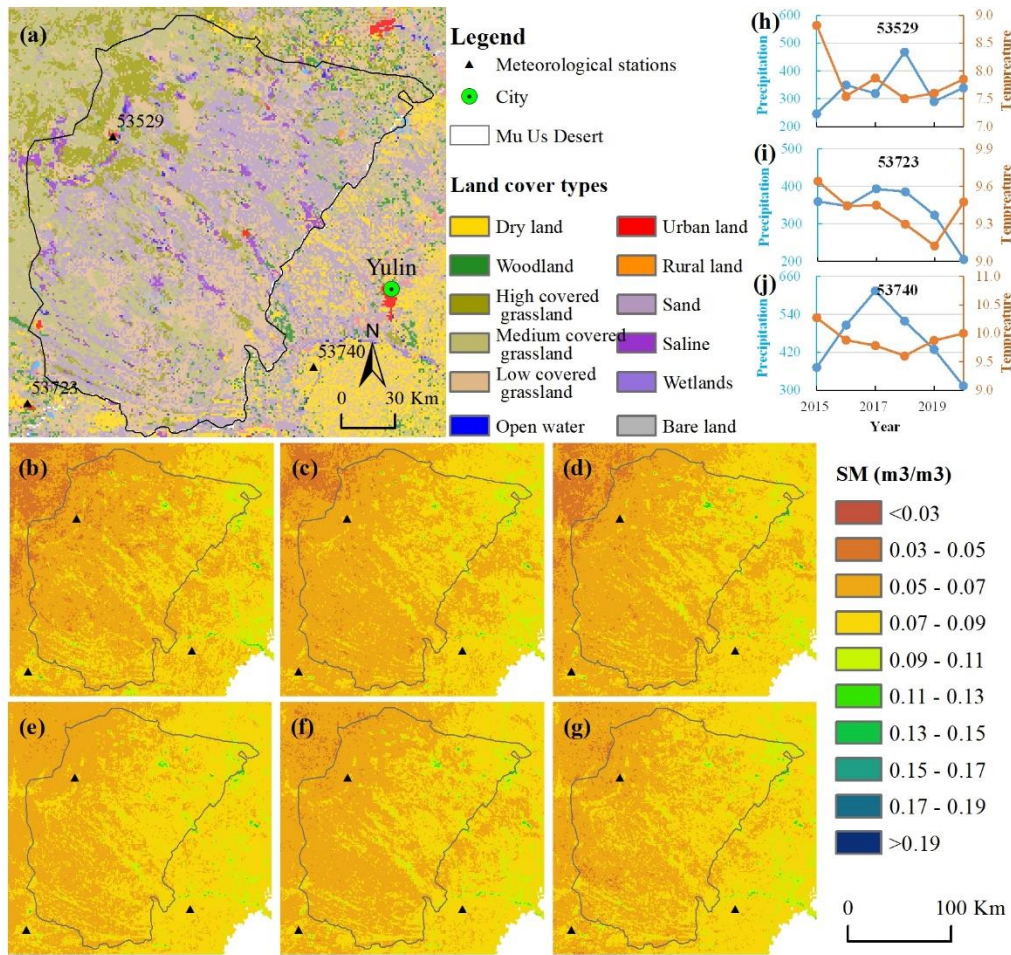
357 overestimated in these regions. In addition, FLDAS SM does not show wetter soil along the river. The spatial patterns of the  
 358 RF-based and XGB-based downscaled SMs are both close to that of the downscaled SM with multiple machine learning  
 359 approaches, however, the the maximum SM based on RF is smaller than the results based on XGB and multi-model  
 360 combination.



361  
 362 **Figure 11: Daily average SM from 2015-2020 in the study area. (a)-(f) are the downscaled SM (1 km), SMAP L3 SM (36 km),**  
 363 **GCOMW/ASMR2 SM (0.1°), C3S SM (0.25°), ERA5 SM (0.1°), FLDAS SM (0.1°), RF-based and XGB-based downscaled SMs (1**  
 364 **km), respectively.**

365 To better demonstrate the differences in SM, a case of the Mu Us Desert was selected (Fig. 12). The Mu Us Desert is  
 366 located in a semi-arid area with annual average precipitation of less than 400 mm, decreasing gradually from southeast to  
 367 northwest. The main types of land cover are grassland and sandy land, and the salinization is serious in a few areas.  
 368 Desertification has been severe for a long time in the past but significantly reversed with artificial afforestation in recent years.

369 SM shows an overall trend of gradual decrease from the southeast to the northwest (Fig. 12 (b)~(g)), which is consistent  
 370 with the distribution of precipitation. The average SM of the same location changes little from year to year. Overall, it is  
 371 relatively large in 2018 and relatively small in 2015, which is roughly consistent with annual precipitation patterns. Land cover  
 372 types also have a certain influence on the spatial difference of SM. The northwestern portion of the Mu Us Desert is mainly  
 373 grassland, which is strongly dependent on precipitation (Fig. 12 (h)). The southeastern area is mainly cultivated land and is  
 374 less affected by precipitation as it relies on pumping groundwater rather than natural precipitation (Fig. 12 (j)).



375

376

Figure 12: Soil moisture estimated for the Mu Us Desert. (a) Land cover distribution over the study area; (b)-(g) annual average SM from 2015-2020; (h)-(j) annual precipitation and annual average temperature of three sites (53529, 53723 and 53740), whose surroundings are mainly grassland, cultivated land, and cultivated land, respectively.

378

379

## 4. Discussion

380

### 4.1 Variable importance assessment

381

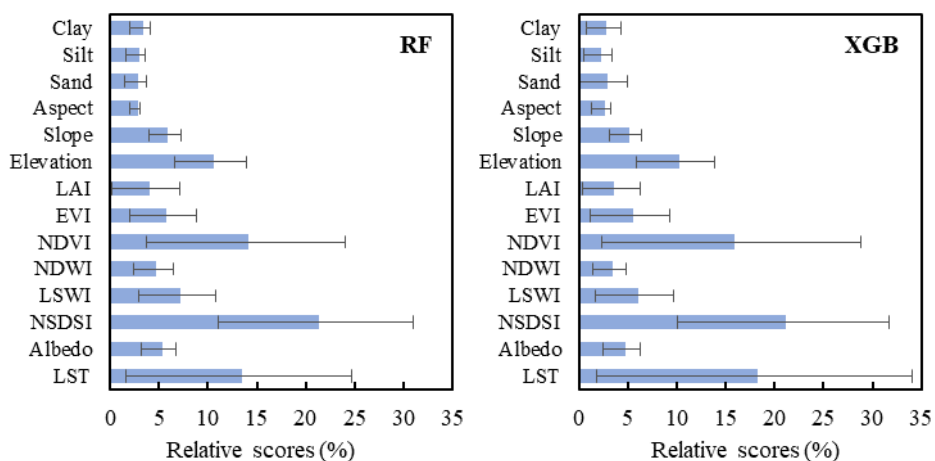
The selection of variables is an important step of a nonlinear regression model. The importance analysis of the variables carried out for this research found that a larger number of variables can improve the regression effect of these models. Due to the variables obtained in this study come from multiple data sources, their preprocessing may affect the construction of regression models and their relationship with SM. Moreover, variables collinearity and hyperparameters also affect the importance relationship of variables. Figure 13 shows the average importance scores of each variable for the RF and XGB models across all available days. The importance scores of different variables in the RF based model and the XGB based model

386

387 are similar. LST and surface albedo both affect surface energy exchange and partition. LST is an important variable in both  
 388 models, which is consistent with the study of Zhao et al. (2018). NSDSI is the most sensitive soil moisture index compared to  
 389 LSWI and NDWI, which was demonstrated in Yue et al. (2019). Topographical factors also exhibit importance on SM,  
 390 especially elevation. NDVI is more sensitive to vegetation index than EVI and LAI. However, their effect was smaller than  
 391 that of soil moisture index. It indicates that the SM inversion based only on LST and VI is inadequate. The influence of soil  
 392 texture (sand, silt and clay) is relatively weak.

393 The standard deviation of the importance scores of each variable is shown with error bars in Fig. 13. Its changes are  
 394 mainly affected by the samples used in the regression model and the temporal variations in surface variables. For static  
 395 variables such as soil structure and topographic factors, the changes in their importance scores mainly depend on the number  
 396 and the location of the samples. Figure 13 also shows that their standard deviation is relatively small. Compared with static  
 397 variables, the standard deviation of the importance scores of dynamic variables is significantly larger, especially for LST and  
 398 LAI. This indicates that it is not reliable to construct a single regression model for a long time series.

399 In general, the variable importance analysis suggests that the selected variables are suitable for the construction of the  
 400 regression model. Moreover, choosing 16 days as a time period to build a regression model benefits from obtaining a sufficient  
 401 number of samples.



402  
 403 **Figure 13: The average importance scores of variables for the RF based approach and XGB based approach. Note: The importance**  
 404 **scores are presented by increase in Node Purity (IncNodePurity) where the sum value is normalized for the RF model; The XGB**  
 405 **model uses Gain to reflect the weight of variables.**

#### 406 4.2 Advantages of model combination

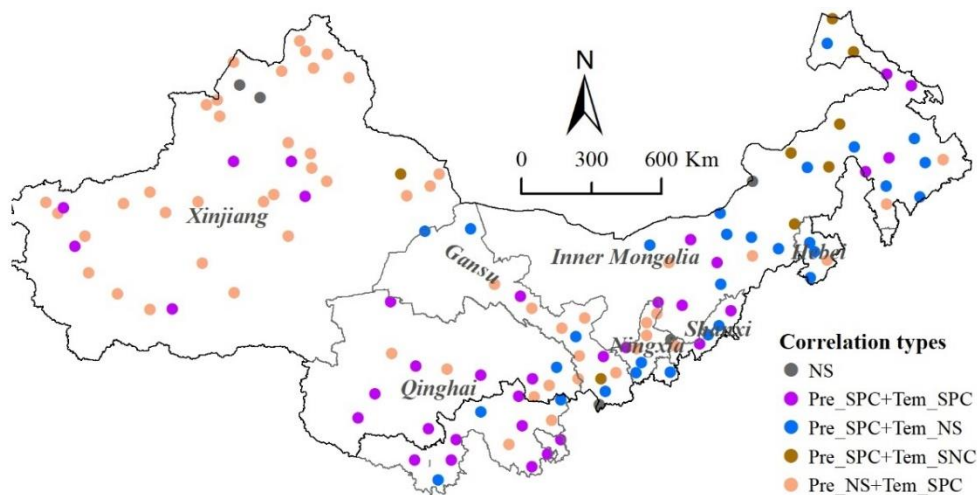
407 Both RF and ANN have been applied to downscale remote sensed SM so far, especially RF (Zhao et al., 2018; Qu et al.,  
 408 2019; Hu et al., 2020). This study showed that the simulation results of ANN have greater uncertainty, and the accuracy is  
 409 generally worse than that of RF (Figs. 4 and 5). The RF algorithm shows a good simulation ability, but in comparison, the

410 XGB algorithm also has a corresponding effect or even higher. We also compared our simulation results combining multiple  
411 models and the RF-based simulation results. The results showed that the combined products have higher accuracy than the RF-  
412 based products, which is mainly reflected in the relatively more reasonable simulation of peaks and valleys (Table 4 and Fig  
413 11). MLR has the worst effect compared to the other four models, which is likely to be affected by variable collinearity. In  
414 fact, many algorithms, especially linear ones, exhibit more or less poor robustness when there is high collinearity between  
415 variables (Dormann et al., 2013; Cammarota and Pinto, 2021). However, fewer explanatory variables often mean less ability  
416 to explain target variables. Several studies have shown that ensemble tree algorithms such as RF and XGB are generally not  
417 affected by variable collinearity (Tomaschek et al., 2018; Chen et al., 2020; Feng et al., 2021).

418 A combination of multiple methods can reduce overfitting and uncertainties for the simulation of long time series (Zanotti  
419 et al., 2019; Yu et al., 2021). The five methods (MLR, SVR, ANN, RF and XGB) in this study have indicated the potential  
420 flaws of a single model. Although the XGB model generally performs better than other models, it has still some shortcomings.  
421 As it can be seen from Figs. 4 and 5, compared with the training accuracy, the test accuracy of the XGB model is significantly  
422 reduced in several periods. This means that the simulation results of the XGB model is likely to have a certain degree of  
423 overfitting. In contrast, the difference between training and test accuracy of the RF model is smaller. It showed better stability  
424 than XGB at several periods (Figs. 4 and 5). The training accuracy of MLR and SVR has a small difference from the test  
425 accuracy, but their overall accuracy is obviously lower (Table 4), which might be due to variable collinearity. Some studies  
426 have proved that SVR may also perform better than ensemble algorithms (Yu et al., 2012; Fan et al., 2018). The fitting effect  
427 of ANN varies greatly in different periods, indicating that its generalization is lower than other models (Piotrowski and  
428 Napiorkowski, 2013). In general, the XGB and RF models provide the best combination of prediction accuracy and stability.

### 429 **4.3 Analysis of the relationship with precipitation and temperature**

430 Unlike predictors such as LST and NDVI that reflect SM status, climatic factors are key drivers of SM variability. To  
431 evaluate the impact of precipitation and temperature on SM, we performed a partial correlation analysis on the data of all  
432 meteorological stations. Figure 14 shows that SM is mainly positively correlated with precipitation and temperature, and a few  
433 regions are significantly negatively correlated with temperature. In terms of spatial distribution, SM of the sites in the eastern  
434 region (including Inner Mongolia Province, Hebei Province and Shanxi Province) is mainly significantly affected by  
435 precipitation. Due to the influence of glaciers and snowmelt, the SM of the sites in the western region (Xinjiang Province and  
436 Gansu Province) is more affected by temperature. In addition, the number of sites with significant positive correlation with  
437 precipitation and temperature is the largest in Qinghai Province. This indicates that precipitation and temperature in the eastern  
438 part of the eastern Tibetan Plateau both have a great influence on SM.



439

440

441

**Figure 14: Partial correlation between monthly downscaled SM and precipitation and temperature (Pre: precipitation; Tem: temperature; NS: Not significance; SPC: Significantly positive correlation; SNC: Significantly negative correlation).**

442

#### 4.4 Uncertainty and Prospects

443

444

445

446

447

448

449

450

451

452

453

While this study greatly improved the spatial resolution of SM data from 2015-2020 in the desertification areas of North China by downscaling SMAP SM products, it still presents some shortcomings. Due to the influence of snow, ice and frozen ground, the number of valid SMAP pixels during cold seasons is usually small, which limits the number of available samples. With a period of 16-day, the number of valid samples may still be less than 100 during cold seasons (Fig. 3). The sample size affects the simulation accuracy. Figures 4 and 5 show that there are seasonal variations in R and RMSE, which is likely to be affected by the sample size. In general, a larger sample size often means more efficient sampling and more reliable results, but not necessarily better evaluation accuracy. Likewise, insufficient samples can sometimes have good evaluation accuracy, although the results are less reliable. In order to reduce the error caused by insufficient samples, this study replaced the periods with less than 100 samples with the model of the previous periods. For this reason, the simulation results sometimes perform poorly during cold seasons (Fig. 9). In addition, the upscaling (from 1 km to 36 km resolution) of surface variables also has a certain impact on the accuracy of the model.

454

455

456

457

458

459

460

461

Our products have a good correlation with the in situ observation data. However, in situ observed SM data are limited in their representation of the entire 1 km × 1 km grid. Figure 6 shows that the evaluation accuracy of different points varies greatly. It indicates that the relationship between in situ observation data and remote sensing SM has great uncertainty due to the influence of scale, and the same conclusion can also be found in some related studies (Zeng et al., 2015; Abbaszadeh et al., 2019; Bai et al., 2019; Liu et al., 2019; Zhang et al., 2020). In addition, due to instrument accuracy and climate change, there are some errors in the in situ observation data, especially at low temperatures. The in situ observed SM data obtained in this paper are relatively limited, and their spatial distribution is concentrated in a certain part of of the study area, which is weak representative. In order to verify the accuracy of the data as much as possible, this study also selected several sets of gridded

462 SM products for comparison. The results showed that our products perform better in temporal variability and spatial patterns  
463 (Figs. 9 and 11).

## 464 **5 Data availability**

465 The codes mainly used in this paper mainly includes sample selection, the building of the optimal regression model and  
466 the result prediction. The downscaled daily SM dataset at 1 km spatial resolution is available at  
467 <https://doi.org/10.6084/m9.figshare.16430478.v6> (Rao et al., 2022). The data maps are all provided in Geotiff format, and the  
468 value has expanded 10,000 times to make them easier to store. The filenames reflect the production date in Julian Day format.

## 469 **6 Conclusions**

470 In this study, an approach was proposed for downscaling 36 km SMAP SM products using MODIS optical products and  
471 other surface variables (mainly topographic data and soil data) based on multiple machine learning methods. Overall, the  
472 regression performance of the five methods is, in order: XGB>RF>SVR>ANN>MLR. Compared with MLR, SVR and ANN,  
473 XGB and RF have much better accuracy, and they were used in combination to produce daily 1 km downscaled SM in a period  
474 of 16 days. The validation shows that the downscaled SM data are highly related to most in situ measured SM. The ubRMSE  
475 with an average of 0.057 m<sup>3</sup>/m<sup>3</sup> is generally less than 0.090 m<sup>3</sup>/m<sup>3</sup> at the Maqu Network. Time series of SM data from in situ  
476 observation sites were also compared. The results show that the downscaled SMs are highly related to SMAP SMs, and provide  
477 a more complete time series and match better with the in situ measured SM. Compared with some commonly used gridded  
478 SM products such as SMAP L2 (1 km or 3 km), GCOMW/ASMR2, C3S, ERA5 and FLDAS SMs, the downscaled SM data  
479 not only have higher spatial resolution, but also have a more reliable accuracy whether in time series or spatial distribution.

480 The maps of downscaled SM show larger values from June to September, which coincides with the vegetation growing  
481 season. The difference in annual mean SM is small. Spatially, SM is relatively large in Qinghai Province and in northeastern  
482 Inner Mongolia, especially in summer. In arid areas such as the Tarim Basin, SM is relatively small throughout the year.  
483 Moreover, precipitation and temperature both have great influence on SM in the study area. Precipitation has a greater impact  
484 on SM in the eastern part of the study area, while the effect of temperature appears to be more pronounced in the west.

485 This approach makes it possible to more accurately assess the soil moisture status in the study area. The results can support  
486 regional agricultural planting and revegetation efforts and can be applied to limit desertification in other areas in the future.

487  
488 **Author contributions.** FW and PR designed the research, developed the methodology, performed the analysis, and wrote the  
489 paper; YW, YL, XW, and ZW edited and revised the paper.

490  
491 **Competing interests.** The authors declare that they have no conflict of interest.



492

493 **Acknowledgements.** This work was supported by the National Key Research and Development Program of China  
494 (2018YFC0408103), the National Pilot Project for Ecological Protection and Restoration of Mountains, Rivers, Forests,  
495 Farmlands, Lakes and Grasslands (Grant No. WR0203A552018), and the Desertification Monitoring Project of National  
496 Forestry and Grass Administration (Grant No. 2020062012). We thank all data providers and the anonymous reviewers for  
497 their detailed and constructive comments.

## 498 **References**

499 Abbaszadeh, P., Moradkhani, H., and Zhan, X.: Downscaling SMAP Radiometer Soil Moisture Over the CONUS Using an  
500 Ensemble Learning Method, *Water Resour. Res.*, 55, 324–344, <https://doi.org/10.1029/2018WR023354>, 2019.

501 Achieng, K. O.: Modelling of soil moisture retention curve using machine learning techniques: Artificial and deep neural  
502 networks vs support vector regression models, *Computers & Geosciences*, 133, 104320,  
503 <https://doi.org/10.1016/j.cageo.2019.104320>, 2019.

504 Ågren, A. M., Larson, J., Paul, S. S., Laudon, H., and Lidberg, W.: Use of multiple LIDAR-derived digital terrain indices and  
505 machine learning for high-resolution national-scale soil moisture mapping of the Swedish forest landscape, *Geoderma*,  
506 404, 115280, <https://doi.org/10.1016/j.geoderma.2021.115280>, 2021.

507 Akoglu, H.: User's guide to correlation coefficients, *Turkish Journal of Emergency Medicine*, 18, 91–93,  
508 <https://doi.org/10.1016/j.tjem.2018.08.001>, 2018.

509 Bai, J., Cui, Q., Zhang, W., and Meng, L.: An Approach for Downscaling SMAP Soil Moisture by Combining Sentinel-1 SAR  
510 and MODIS Data, *Remote Sensing*, 11, 2736, <https://doi.org/10.3390/rs11232736>, 2019.

511 Belgiu, M. and Drăguț, L.: Random forest in remote sensing: A review of applications and future directions, 114, 24–31,  
512 <https://doi.org/10.1016/j.isprsjprs.2016.01.011>, 2016.

513 Cammarota, C. and Pinto, A.: Variable selection and importance in presence of high collinearity: an application to the  
514 prediction of lean body mass from multi-frequency bioelectrical impedance, *Journal of Applied Statistics*, 48, 1644–1658,  
515 <https://doi.org/10.1080/02664763.2020.1763930>, 2021.

516 Chen, H., Chen, H., Liu, Z., Sun, X., and Zhou, R.: Analysis of Factors Affecting the Severity of Automated Vehicle Crashes  
517 Using XGBoost Model Combining POI Data, *Journal of Advanced Transportation*, 2020, 1–12,  
518 <https://doi.org/10.1155/2020/8881545>, 2020.

519 Chen, T. and Guestrin, C.: XGBoost: A Scalable Tree Boosting System, in: *Proceedings of the 22nd ACM SIGKDD*  
520 *International Conference on Knowledge Discovery and Data Mining, KDD '16: The 22nd ACM SIGKDD International*  
521 *Conference on Knowledge Discovery and Data Mining, San Francisco California USA*, 785–794,  
522 <https://doi.org/10.1145/2939672.2939785>, 2016.

523 Chen, Y., Feng, X., and Fu, B.: An improved global remote-sensing-based surface soil moisture (RSSSM) dataset covering  
524 2003–2018, *Earth Syst. Sci. Data*, 13, 1–31, <https://doi.org/10.5194/essd-13-1-2021>, 2021.

- 525 De Santis, D., Biondi, D., Crow, W. T., Camici, S., Modanesi, S., Brocca, L., and Massari, C.: Assimilation of Satellite Soil  
526 Moisture Products for River Flow Prediction: An Extensive Experiment in Over 700 Catchments Throughout Europe,  
527 *Water Res.*, 57, <https://doi.org/10.1029/2021WR029643>, 2021.
- 528 Del Frate, F., Ferrazzoli, P., and Schiavon, G.: Retrieving soil moisture and agricultural variables by microwave radiometry  
529 using neural networks, *Remote Sensing of Environment*, 84, 174–183, [https://doi.org/10.1016/S0034-4257\(02\)00105-0](https://doi.org/10.1016/S0034-4257(02)00105-0),  
530 2003.
- 531 Demarchi, L., Kania, A., Ciężkowski, W., Piórkowski, H., Oświecimska-Piasko, Z., and Chormański, J.: Recursive Feature  
532 Elimination and Random Forest Classification of Natura 2000 Grasslands in Lowland River Valleys of Poland Based on  
533 Airborne Hyperspectral and LiDAR Data Fusion, *Remote Sensing*, 12, 1842, <https://doi.org/10.3390/rs12111842>, 2020.
- 534 Dormann, C. F., Elith, J., Bacher, S., Buchmann, C., Carl, G., Carré, G., Marquéz, J. R. G., Gruber, B., Lafourcade, B., Leitão,  
535 P. J., Münkemüller, T., McClean, C., Osborne, P. E., Reineking, B., Schröder, B., Skidmore, A. K., Zurell, D., and  
536 Lautenbach, S.: Collinearity: a review of methods to deal with it and a simulation study evaluating their performance,  
537 *Ecography*, 36, 27–46, <https://doi.org/10.1111/j.1600-0587.2012.07348.x>, 2013.
- 538 Elshorbagy, A. and Parasuraman, K.: On the relevance of using artificial neural networks for estimating soil moisture content,  
539 *Journal of Hydrology*, 362, 1–18, <https://doi.org/10.1016/j.jhydrol.2008.08.012>, 2008.
- 540 Fan, J., Yue, W., Wu, L., Zhang, F., Cai, H., Wang, X., Lu, X., and Xiang, Y.: Evaluation of SVM, ELM and four tree-based  
541 ensemble models for predicting daily reference evapotranspiration using limited meteorological data in different climates  
542 of China, *Agricultural and Forest Meteorology*, 263, 225–241, <https://doi.org/10.1016/j.agrformet.2018.08.019>, 2018.
- 543 Fan, J., Zheng, J., Wu, L., and Zhang, F.: Estimation of daily maize transpiration using support vector machines, extreme  
544 gradient boosting, artificial and deep neural networks models, *Agricultural Water Management*, 245, 106547,  
545 <https://doi.org/10.1016/j.agwat.2020.106547>, 2021.
- 546 Fang, B. and Lakshmi, V.: Soil moisture at watershed scale: Remote sensing techniques, *Journal of Hydrology*, 516, 258–272,  
547 <https://doi.org/10.1016/j.jhydrol.2013.12.008>, 2014.
- 548 Fang, B., Lakshmi, V., Bindlish, R., Jackson, T. J., Cosh, M., and Basara, J.: Passive Microwave Soil Moisture Downscaling  
549 Using Vegetation Index and Skin Surface Temperature, *Vadose Zone Journal*, 12, vzj2013.05.0089er,  
550 <https://doi.org/10.2136/vzj2013.05.0089er>, 2013.
- 551 Feng, R., Dario, G., and Balling, N.: Imputation of missing well log data by random forest and its uncertainty analysis, 152, 9,  
552 <https://doi.org/10.1016/j.cageo.2021.104763>, 2021.
- 553 Gu, Y., Hunt, E., Wardlow, B., Basara, J. B., Brown, J. F., and Verdin, J. P.: Evaluation of MODIS NDVI and NDWI for  
554 vegetation drought monitoring using Oklahoma Mesonet soil moisture data, *Geophys. Res. Lett.*, 35, L22401,  
555 <https://doi.org/10.1029/2008GL035772>, 2008.
- 556 Hu, F., Wei, Z., Zhang, W., Dorjee, D., and Meng, L.: A spatial downscaling method for SMAP soil moisture through visible  
557 and shortwave-infrared remote sensing data, *Journal of Hydrology*, 590, 125360,  
558 <https://doi.org/10.1016/j.jhydrol.2020.125360>, 2020.
- 559 Im, J., Park, S., Rhee, J., Baik, J., and Choi, M.: Downscaling of AMSR-E soil moisture with MODIS products using machine  
560 learning approaches, *Environ Earth Sci*, 75, 1120, <https://doi.org/10.1007/s12665-016-5917-6>, 2016.

- 561 Kang, J., Jin, R., Li, X., Ma, C., Qin, J., and Zhang, Y.: High spatio-temporal resolution mapping of soil moisture by integrating  
562 wireless sensor network observations and MODIS apparent thermal inertia in the Babao River Basin, China, *Remote*  
563 *Sensing of Environment*, 191, 232–245, <https://doi.org/10.1016/j.rse.2017.01.027>, 2017.
- 564 Khan, F., Kanwal, S., Alamri, S., and Mumtaz, B.: Hyper-Parameter Optimization of Classifiers, Using an Artificial Immune  
565 Network and Its Application to Software Bug Prediction, 8, 11, <https://doi.org/10.1109/ACCESS.2020.2968362>, 2020.
- 566 Klein, A., Falkner, S., Bartels, S., Hennig, P., and Hutter, F.: Fast Bayesian Optimization of Machine Learning  
567 Hyperparameters on Large Datasets, <https://doi.org/10.48550/arXiv.1605.07079>, 2017.
- 568 Kovalev, M. S. and Utkin, L. V.: A robust algorithm for explaining unreliable machine learning survival models using the  
569 Kolmogorov–Smirnov bounds, *Neural Networks*, 132, 1–18, <https://doi.org/10.1016/j.neunet.2020.08.007>, 2020.
- 570 Lievens, H., Verhoest, N. E. C., De Keyser, E., Vernieuwe, H., Matgen, P., Álvarez-Mozos, J., and De Baets, B.: Effective  
571 roughness modelling as a tool for soil moisture retrieval from C- and L-band SAR, *Hydrol. Earth Syst. Sci.*, 15, 151–162,  
572 <https://doi.org/10.5194/hess-15-151-2011>, 2011.
- 573 Lin, W., Gao, J., Wang, B., and Hong, Q.: An Improved Random Forest Classifier for Imbalanced Learning, in: 2021 IEEE  
574 International Conference on Artificial Intelligence and Computer Applications (ICAICA), 2021 IEEE International  
575 Conference on Artificial Intelligence and Computer Applications (ICAICA), Dalian, China, 703–707,  
576 <https://doi.org/10.1109/ICAICA52286.2021.9497933>, 2021.
- 577 Liu, J., Chai, L., Lu, Z., Liu, S., Qu, Y., Geng, D., Song, Y., Guan, Y., Guo, Z., Wang, J., and Zhu, Z.: Evaluation of SMAP,  
578 SMOS-IC, FY3B, JAXA, and LPRM Soil Moisture Products over the Qinghai-Tibet Plateau and Its Surrounding Areas,  
579 *Remote Sensing*, 11, 792, <https://doi.org/10.3390/rs11070792>, 2019.
- 580 Liu, J., Chai, L., Dong, J., Zheng, D., Wigneron, J.-P., Liu, S., Zhou, J., Xu, T., Yang, S., Song, Y., Qu, Y., and Lu, Z.:  
581 Uncertainty analysis of eleven multisource soil moisture products in the third pole environment based on the three-corned  
582 hat method, *Remote Sensing of Environment*, 255, 112225, <https://doi.org/10.1016/j.rse.2020.112225>, 2021.
- 583 Liu, Y., Yao, L., Jing, W., Di, L., Yang, J., and Li, Y.: Comparison of two satellite-based soil moisture reconstruction  
584 algorithms: A case study in the state of Oklahoma, USA, *Journal of Hydrology*, 590, 125406,  
585 <https://doi.org/10.1016/j.jhydrol.2020.125406>, 2020.
- 586 Ma, H., Zeng, J., Chen, N., Zhang, X., Cosh, M. H., and Wang, W.: Satellite surface soil moisture from SMAP, SMOS,  
587 AMSR2 and ESA CCI: A comprehensive assessment using global ground-based observations, *Remote Sensing of*  
588 *Environment*, 231, 111215, <https://doi.org/10.1016/j.rse.2019.111215>, 2019.
- 589 Ma, M., Zhao, G., He, B., Li, Q., Dong, H., Wang, S., and Wang, Z.: XGBoost-based method for flash flood risk assessment,  
590 *Journal of Hydrology*, 598, 126382, <https://doi.org/10.1016/j.jhydrol.2021.126382>, 2021.
- 591 Mallick, K., Bhattacharya, B. K., and Patel, N. K.: Estimating volumetric surface moisture content for cropped soils using a  
592 soil wetness index based on surface temperature and NDVI, *Agricultural and Forest Meteorology*, 149, 1327–1342,  
593 <https://doi.org/10.1016/j.agrformet.2009.03.004>, 2009.
- 594 Meng, X., Mao, K., Meng, F., Shi, J., Zeng, J., Shen, X., Cui, Y., Jiang, L., and Guo, Z.: A fine-resolution soil moisture dataset  
595 for China in 2002–2018, *Geosciences – Geophysics*, <https://doi.org/10.5194/essd-2020-292>, 2020.

- 596 Mohana, R. M., Reddy, C. K. K., Anisha, P. R., and Murthy, B. V. R.: Random forest algorithms for the classification of tree-  
597 based ensemble, *Materials Today: Proceedings*, S2214785321008853, <https://doi.org/10.1016/j.matpr.2021.01.788>, 2021.
- 598 O'Neill, P., Entekhabi, D., Njoku, E., and Kellogg, K.: The NASA Soil Moisture Active Passive (SMAP) mission: Overview,  
599 in: *2010 IEEE International Geoscience and Remote Sensing Symposium, IGARSS 2010 - 2010 IEEE International*  
600 *Geoscience and Remote Sensing Symposium, Honolulu, HI, USA, 3236–3239*,  
601 <https://doi.org/10.1109/IGARSS.2010.5652291>, 2010.
- 602 Peng, J., Loew, A., Merlin, O., and Verhoest, N. E. C.: A review of spatial downscaling of satellite remotely sensed soil  
603 moisture: Downscale Satellite-Based Soil Moisture, *Rev. Geophys.*, 55, 341–366,  
604 <https://doi.org/10.1002/2016RG000543>, 2017.
- 605 Peng, J., Albergel, C., Balenzano, A., Brocca, L., Cartus, O., Cosh, M. H., Crow, W. T., Dabrowska-Zielinska, K., Dadson, S.,  
606 Davidson, M. W. J., de Rosnay, P., Dorigo, W., Gruber, A., Hagemann, S., Hirschi, M., Kerr, Y. H., Lovergine, F.,  
607 Mahecha, M. D., Marzahn, P., Mattia, F., Musial, J. P., Preuschmann, S., Reichle, R. H., Satalino, G., Silgram, M., van  
608 Bodegom, P. M., Verhoest, N. E. C., Wagner, W., Walker, J. P., Wegmüller, U., and Loew, A.: A roadmap for high-  
609 resolution satellite soil moisture applications – confronting product characteristics with user requirements, 15, 2021.
- 610 Piles, M., Petropoulos, G. P., Sánchez, N., González-Zamora, Á., and Ireland, G.: Towards improved spatio-temporal  
611 resolution soil moisture retrievals from the synergy of SMOS and MSG SEVIRI spaceborne observations, *Remote*  
612 *Sensing of Environment*, 180, 403–417, <https://doi.org/10.1016/j.rse.2016.02.048>, 2016.
- 613 Piotrowski, A. P. and Napiorkowski, J. J.: A comparison of methods to avoid overfitting in neural networks training in the  
614 case of catchment runoff modelling, *Journal of Hydrology*, 476, 97–111, <https://doi.org/10.1016/j.jhydrol.2012.10.019>,  
615 2013.
- 616 Qu, Y., Zhu, Z., Chai, L., Liu, S., Montzka, C., Liu, J., Yang, X., Lu, Z., Jin, R., Li, X., Guo, Z., and Zheng, J.: Rebuilding a  
617 Microwave Soil Moisture Product Using Random Forest Adopting AMSR-E/AMSR2 Brightness Temperature and SMAP  
618 over the Qinghai–Tibet Plateau, China, *Remote Sensing*, 11, 683, <https://doi.org/10.3390/rs11060683>, 2019.
- 619 Rahimzadeh-Bajgirani, P., Berg, A. A., Champagne, C., and Omasa, K.: Estimation of soil moisture using optical/thermal  
620 infrared remote sensing in the Canadian Prairies, *ISPRS Journal of Photogrammetry and Remote Sensing*, 83, 94–103,  
621 <https://doi.org/10.1016/j.isprsjprs.2013.06.004>, 2013.
- 622 Rao, P., Jiang, W., Hou, Y., Chen, Z., and Jia, K.: Dynamic Change Analysis of Surface Water in the Yangtze River Basin  
623 Based on MODIS Products, *Remote Sensing*, 10, 1025, <https://doi.org/10.3390/rs10071025>, 2018.
- 624 Rao, P., Wang, Yicheng, Wang, Fang, Liu, Yang, Wang, Xiaoya, and Wang, Zhu: Daily soil moisture mapping at 1 km  
625 resolution based on SMAP data for desertification areas in Northern China.,  
626 <https://doi.org/10.6084/m9.figshare.16430478.v6>, 2022.
- 627 Sandholt, I., Rasmussen, K., and Andersen, J.: A simple interpretation of the surface temperature/vegetation index space for  
628 assessment of surface moisture status, *Remote Sensing of Environment*, 79, 213–224, [https://doi.org/10.1016/S0034-4257\(01\)00274-7](https://doi.org/10.1016/S0034-4257(01)00274-7), 2002.
- 630 Shangguan, W., Dai, Y., Liu, B., Ye, A., and Yuan, H.: A soil particle-size distribution dataset for regional land and climate  
631 modelling in China, *Geoderma*, 171–172, 85–91, <https://doi.org/10.1016/j.geoderma.2011.01.013>, 2012.

- 632 Shi, R., Xu, X., Li, J., and Li, Y.: Prediction and analysis of train arrival delay based on XGBoost and Bayesian optimization,  
633 Applied Soft Computing, 109, 107538, <https://doi.org/10.1016/j.asoc.2021.107538>, 2021.
- 634 Sun, D., Xu, J., Wen, H., and Wang, D.: Assessment of landslide susceptibility mapping based on Bayesian hyperparameter  
635 optimization: A comparison between logistic regression and random forest, 281, 12,  
636 <https://doi.org/10.1016/j.enggeo.2020.105972>, 2021.
- 637 Sun, L., Sun, R., Li, X., Liang, S., and Zhang, R.: Monitoring surface soil moisture status based on remotely sensed surface  
638 temperature and vegetation index information, Agricultural and Forest Meteorology, 166–167, 175–187,  
639 <https://doi.org/10.1016/j.agrformet.2012.07.015>, 2012.
- 640 Tomaschek, F., Hendrix, P., and Baayen, R. H.: Strategies for addressing collinearity in multivariate linguistic data, Journal  
641 of Phonetics, 71, 249–267, <https://doi.org/10.1016/j.wocn.2018.09.004>, 2018.
- 642 Wagner, W., Hahn, S., Kidd, R., Melzer, T., Bartalis, Z., Hasenauer, S., Figa-Saldaña, J., de Rosnay, P., Jann, A., Schneider,  
643 S., Komma, J., Kubu, G., Brugger, K., Aubrecht, C., Züger, J., Gangkofner, U., Kienberger, S., Brocca, L., Wang, Y.,  
644 Blöschl, G., Eitzinger, J., and Steinnocher, K.: The ASCAT Soil Moisture Product: A Review of its Specifications,  
645 Validation Results, and Emerging Applications, *metz*, 22, 5–33, <https://doi.org/10.1127/0941-2948/2013/0399>, 2013.
- 646 Wang, G., Zhang, X., Yinglan, A., Duan, L., Xue, B., and Liu, T.: A spatio-temporal cross comparison framework for the  
647 accuracies of remotely sensed soil moisture products in a climate-sensitive grassland region, Journal of Hydrology, 597,  
648 126089, <https://doi.org/10.1016/j.jhydrol.2021.126089>, 2021.
- 649 Wang, S., Liu, S., Zhang, J., Che, X., Yuan, Y., Wang, Z., and Kong, D.: A new method of diesel fuel brands identification:  
650 SMOTE oversampling combined with XGBoost ensemble learning, Fuel, 282, 118848,  
651 <https://doi.org/10.1016/j.fuel.2020.118848>, 2020.
- 652 Wang, T., Yang, D., Fang, B., Yang, W., Qin, Y., and Wang, Y.: Data-driven mapping of the spatial distribution and potential  
653 changes of frozen ground over the Tibetan Plateau, Science of The Total Environment, 649, 515–525,  
654 <https://doi.org/10.1016/j.scitotenv.2018.08.369>, 2019.
- 655 Wang, X., Xie, H., Guan, H., and Zhou, X.: Different responses of MODIS-derived NDVI to root-zone soil moisture in semi-  
656 arid and humid regions, Journal of Hydrology, 340, 12–24, <https://doi.org/10.1016/j.jhydrol.2007.03.022>, 2007.
- 657 Yao, P., Shi, J., Zhao, T., Lu, H., and Al-Yaari, A.: Rebuilding Long Time Series Global Soil Moisture Products Using the  
658 Neural Network Adopting the Microwave Vegetation Index, Remote Sensing, 9, 35, <https://doi.org/10.3390/rs9010035>,  
659 2017.
- 660 Yu, H., Wu, Y., Niu, L., Chai, Y., Feng, Q., Wang, W., and Liang, T.: A method to avoid spatial overfitting in estimation of  
661 grassland above-ground biomass on the Tibetan Plateau, Ecological Indicators, 125, 107450,  
662 <https://doi.org/10.1016/j.ecolind.2021.107450>, 2021.
- 663 Yu, Z., Liu, D., Lü, H., Fu, X., Xiang, L., and Zhu, Y.: A multi-layer soil moisture data assimilation using support vector  
664 machines and ensemble particle filter, Journal of Hydrology, 475, 53–64, <https://doi.org/10.1016/j.jhydrol.2012.08.034>,  
665 2012.

- 666 Yue, J., Tian, J., Tian, Q., Xu, K., and Xu, N.: Development of soil moisture indices from differences in water absorption  
667 between shortwave-infrared bands, *ISPRS Journal of Photogrammetry and Remote Sensing*, 154, 216–230,  
668 <https://doi.org/10.1016/j.isprsjprs.2019.06.012>, 2019.
- 669 Zanotti, C., Rotiroti, M., Sterlacchini, S., Cappellini, G., Fumagalli, L., Stefania, G. A., Nannucci, M. S., Leoni, B., and Bonomi,  
670 T.: Choosing between linear and nonlinear models and avoiding overfitting for short and long term groundwater level  
671 forecasting in a linear system, *Journal of Hydrology*, 578, 124015, <https://doi.org/10.1016/j.jhydrol.2019.124015>, 2019.
- 672 Zawadzki, J. and Kędzior, M.: Soil moisture variability over Odra watershed: Comparison between SMOS and GLDAS data,  
673 *International Journal of Applied Earth Observation and Geoinformation*, 45, 110–124,  
674 <https://doi.org/10.1016/j.jag.2015.03.005>, 2016.
- 675 Zeng, J., Li, Z., Chen, Q., Bi, H., Qiu, J., and Zou, P.: Evaluation of remotely sensed and reanalysis soil moisture products  
676 over the Tibetan Plateau using in-situ observations, *Remote Sensing of Environment*, 163, 91–110,  
677 <https://doi.org/10.1016/j.rse.2015.03.008>, 2015.
- 678 Zhang, P., Zheng, D., van der Velde, R., Wen, J., Zeng, Y., Wang, X., Wang, Z., Chen, J., and Su, Z.: Status of the Tibetan  
679 Plateau observatory (Tibet-Obs) and a 10-year (2009–2019) surface soil moisture dataset, *Hydrology and Soil Science –*  
680 *Hydrology*, <https://doi.org/10.5194/essd-2020-209>, 2020.
- 681 Zhao, W. and Li, A.: A Downscaling Method for Improving the Spatial Resolution of AMSR-E Derived Soil Moisture Product  
682 Based on MSG-SEVIRI Data, *Remote Sensing*, 5, 6790–6811, <https://doi.org/10.3390/rs5126790>, 2013.
- 683 Zhao, W., Li, A., and Zhao, T.: Potential of Estimating Surface Soil Moisture With the Triangle-Based Empirical Relationship  
684 Model, *IEEE Trans. Geosci. Remote Sensing*, 55, 6494–6504, <https://doi.org/10.1109/TGRS.2017.2728815>, 2017.
- 685 Zhao, W., Sánchez, N., Lu, H., and Li, A.: A spatial downscaling approach for the SMAP passive surface soil moisture product  
686 using random forest regression, *Journal of Hydrology*, 563, 1009–1024, <https://doi.org/10.1016/j.jhydrol.2018.06.081>,  
687 2018.
- 688